J. Fluid Mech. (2026), *vol.* 1043, A23, doi:10.1017/jfm.2026.12015

JFM PAPERS

Broadband absorption of ocean wave energy using a graded array of heaving buoys in three dimensions

Amy-Rose Westcott[1], **Luke G. Bennetts**[2], **Nataliia Y. Sergiienko**[3], **Benjamin S. Cazzolato**[3] and **Malte A. Peter**[4,5]

[1]School of Mathematical Sciences, Adelaide University, Adelaide, SA 5005, Australia

[2]School of Mathematics and Statistics, The University of Melbourne, Melbourne, VIC 3010, Australia

[3]School of Electrical and Mechanical Engineering, Adelaide University, Adelaide, SA 5005, Australia

[4]Institute of Mathematics, University of Augsburg, Augsburg 86135, Germany

[5]Centre for Advanced Analytics and Predictive Sciences, University of Augsburg, Augsburg 86135, Germany

Corresponding authors: Amy-Rose Westcott, amy-rose.westcott@adelaide.edu.au; Luke G. Bennetts, luke.bennetts@unimelb.edu.au

(Received 18 February 2026 UTC; revised 29 June 2026 UTC; accepted 7 August 2026 UTC)

The generation of renewable power from ocean waves at a commercial scale requires arrays of wave energy converters (WECs) to be designed for efficient power capture over broad frequency bands and a wide range of incident wave directions. Here, array designs are developed in a three-dimensional model based on linear potential-flow theory, by arranging heaving-buoy-type WECs into rows, and spatially grading the resonant properties of successive rows via linear spring–damper power take-off (PTO) mechanisms. The grading leverages theories for rainbow reflection and rainbow absorption, and involves analyses of Bloch waves and pole–zero pairs in complex frequency space to inform the array layout and choice of PTO parameters. The spacing within an array alters the resonant properties of the rows and the behaviour of higher-order passbands, which has implications for the efficiency of an array. Strategies are developed to grade arrays composed of rows with infinitely many WECs, for efficient, broadband absorption over a broad target frequency range, and average absorptions exceeding 90 % are achieved over a wide range of wave directions. The strategies are applied to finite arrays, which demonstrate broadband absorption in directionally spread irregular sea states, and are shown to outperform the absorption of uniform arrays across a wide range of peak periods.

Key words: wave-structure interactions, wave scattering, surface gravity waves

© The Author(s), 2026. Published by Cambridge University Press. This is an Open Access article, distributed under the terms of the Creative Commons Attribution licence (https://creativecommons.org/licenses/by/4.0/), which permits unrestricted re-use, distribution and reproduction, provided the original article is properly cited.

https://doi.org/10.1017/jfm.2026.12015

1. Introduction

Renewable power from ocean waves is characterised by high energy density and availability, in proximity to almost half of the global population (Coe *et al.* 2021). Wave energy converters (WECs) are designed to harness this power, but are yet to reach commercial viability, despite the development of many different concepts (Guo & Ringwood 2021). Heaving buoys are a popular type of WEC that convert power at maximum efficiency when tuned to resonate via an attached power take-off (PTO) mechanism (Falnes 2005). However, like many other WECs, heaving buoys have relatively narrow resonance bandwidths compared to ocean waves (Pecher & Kofoed 2017), for which wave periods from 5–20 s are feasible for power capture (Coe *et al.* 2021).

WECs will need to be deployed in arrays that operate at high efficiency to reach economic viability through reducing the cost of power generated per ocean area, and the installation, operations and maintenance cost per WEC (Ning & Ding 2022; Ringwood *et al.* 2023). The power captured by arrays is increased by optimising the WEC geometry (Edwards & Yue 2022), layout (Göteman *et al.* 2020) or PTO parameters (Sheng & Lewis 2016; Blanco *et al.* 2025), preferably in combination (Wilks *et al.* 2025) for a given sea state. However, given the inherent irregularity and variability of wave climates (Ning & Ding 2022), and the sensitivity of arrays to directionality (Gallutia *et al.* 2022), it is likely that control strategies will be necessary to achieve the broadband absorption (high efficiency over broad frequency bands, i.e. resulting in the capture of high proportions of incoming ocean wave spectra) required for cost-effectiveness (Pecher & Kofoed 2017; Coe *et al.* 2021).

Developing control strategies to adjust the PTO parameters according to predicted sea states is an active research topic, with most models based on linear theory (Ringwood *et al.* 2023). The interdependence between the hydrodynamic interactions, array layout and control strategy makes dynamic control (changing WEC properties in time according to the incoming waves) highly complex (Ringwood 2025), which further requires sophisticated PTO mechanisms (Ning & Ding 2022), accurate wave prediction, is sensitive to model errors, and increases overall cost (Pecher & Kofoed 2017). Therefore, there is a strong demand to design arrays that maintain high efficiency without requiring repeated adjustments based on short-term forecasting (Korde & Ringwood 2016; Pecher & Kofoed 2017).

Broadband capture of ocean wave energy by graded arrays has been proposed based on metamaterial 'rainbow' theories for the controlled spatial separation and amplification of the different frequency components of incoming waves (Davies *et al.* 2025). The concept has recently been demonstrated using linear theory, but restricted to two-dimensional (2-D) models for simplicity (Wilks *et al.* 2022; Westcott *et al.* 2024). It involves preventing transmission of targeted wave frequencies through the array by manipulating the underlying local band structures to create rainbow reflection (Wilks *et al.* 2022; Westcott *et al.* 2024). Grading generates a frequency-dependent series of near-resonant responses as the incident wave energy is selectively slowed according to frequency, and accumulates at locations in the array associated with cut-off points, which are defined by the local periodicity, and spatially controlled through the WEC resonances (Bennetts *et al.* 2018). The localised amplifications are captured via the PTO damping, which is chosen to minimise the amplitude of reflected waves for rainbow absorption (Wilks *et al.* 2022; Westcott *et al.* 2024).

Wilks *et al.* (2022) considered heaving-buoy-type WECs surrounded by rigid vertical barriers, which could potentially be realised by integrating oscillating water columns into breakwaters (e.g. Zhao *et al.* 2023; Hu *et al.* 2025). By grading the barriers and using

https://doi.org/10.1017/jfm.2026.12015

an optimisation algorithm, they achieved 98.2 % average absorption of 4–8 s waves. In contrast, Westcott *et al.* (2024) did not include any surrounding structures, and graded the resonances of heaving-buoy WEC arrays via PTO spring terms, thereby harnessing destructive wave interactions to create a series of overlapping, 'local bandgaps' (where the resonance of a WEC inhibits propagation of wave energy). They added PTO damping to capture the spatially controlled amplifications, reaching near-perfect absorption (>99 %) of 10–20 s waves with five WECs after optimisation.

In this study, we make the major next step of taking the concepts of rainbow reflection and absorption to WEC arrays in three-dimensional (3-D) water domains. We follow the approach of Westcott *et al.* (2024), by considering arrays of heaving buoys and grading their resonant properties using the PTO spring terms. We show that the general approach developed in two dimensions can be extended to three dimensions by arranging the array into rows of identical and equally spaced WECs (figure 1; the rows are known as diffraction gratings in some contexts). In particular, the periodic distribution of WECs in each row creates constructive interference in a finite number of directions (which depend on the incident angle, frequency and periodicity length), so that the scattering properties of each row can be described in terms of a discrete directional spectrum (Falnes & Budal 1982). Established methods are applied, and provide a computationally efficient basis for grading the array, which utilises a Bloch wave analysis and reflection and transmission properties to inform the array design (Bennetts & Squire 2009; Peter & Meylan 2010). We show that the approach generates broadband absorption of up to ≈ 95 % over the targeted frequency range with six rows and without using an optimisation algorithm. Moreover, we show that the approach is robust to the wave direction, as the underlying local bandgaps extend over wide incident angle ranges. We also show that the grading strategy holds for finite arrays of only tens of WECs.

The model and solution method are introduced in §§ 2 and 3, respectively. The method is adapted from methods used for electromagnetic waves (e.g. McPhedran *et al.* 1999), acoustics (e.g. Mulholland & Heckl 1994) and water waves in the marginal ice zone (e.g. Chou 1998; Bennetts *et al.* 2010), but is given in detail here as a basis to develop the theory for grading for an array of WECs (§ 4.1). A Bloch wave analysis is used to link underlying band structures (passbands and bandgaps) to the reflection and transmission of the array, which are connected to the resonant properties of each row of WECs in complex frequency space (§ 4.2). The PTO springs are graded for rainbow reflection, and the PTO damping is chosen to generate near-zeros in reflection for rainbow absorption (§ 4.3). Strategies are transferred to finite arrays, where the efficient, broadband absorption of a graded array is demonstrated in directionally spread, irregular sea states, and compared to the absorption of uniform arrays (§ 4.4). Recommendations for practical next steps are given in § 5.

2. Preliminaries

Consider a 3-D water domain Ω containing an array of WECs, where each WEC consists of a floating buoy and a linear spring–damper PTO mechanism that moors it to the seabed (figure 1). The buoys are identical truncated vertical cylinders, with radius L, height $2L$ and draught L. They are constrained to move in heave only. Let the Cartesian coordinate system (x, y, z) denote locations in the water domain, such that (x, y) is the horizontal coordinate, and z is the vertical coordinate, which points upwards and has its origin at the still-water level. The water domain is unbounded in the horizontal direction, $-\infty < x, y < \infty$, and bounded below by a flat impermeable seabed at $z = -h$. Away from the WECs, the water is bounded above by a moving free surface $z = \hat{\eta}(x, y, t)$, where t denotes time, such that $\hat{\eta} \equiv 0$ in equilibrium.

https://doi.org/10.1017/jfm.2026.12015

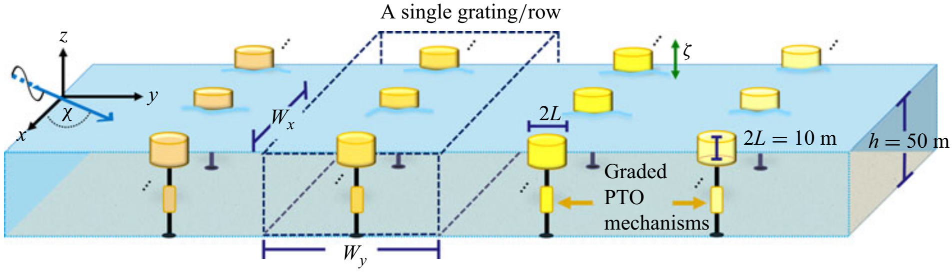

Figure 1. The graded array contains finitely many rows in the y-direction, each consisting of infinitely many WECs (periodicity length W_x). The incident wave travels from left to right at an angle of χ rad to the x-axis. (Note that the axes are rotated by 90° in the clockwise direction to aid illustration.)

The WECs are arranged into K rows, where each row initially contains an infinite number of identical WECs (identical PTO parameters, as well as buoys) in a straight line, and with uniform spacing between adjacent WECs (figure 1). Without loss of generality, let the rows be aligned parallel to the x-axis (rotated by 90° in the clockwise direction in figure 1), and let W_x denote the centre-to-centre spacing between adjacent WECs in a row. The spacing between adjacent rows is also uniform, and the centre-to-centre row spacing is denoted W_y. The rows are indexed $i \in \{1, 2, \ldots, K\}$ in ascending order along the the y-axis, and the WECs in each row are indexed $j \in \mathbb{Z}$ in ascending order along the x-axis. Let one buoy in the first row have its centre in the horizontal plane coincide with the origin $(x, y) = (0, 0)$. Then the WEC array occupies the water surface defined by the set

$$\Gamma = \{(x, y) : (x - j\, W_x)^2 + (y - i\, W_y + W_y)^2 \le L^2 \ \text{ for } i \in [1, 2, \ldots, K] \text{ and } j \in \mathbb{Z}\}. \tag{2.1}$$

The heave motion of the jth buoy in the ith row is denoted $\xi_{i,j}(t)$.

Motions of the coupled water and WEC array system are excited by an ambient incident wave with amplitude A^{inc}, propagating from $y \to -\infty$ (the left of the array in figure 1). The water motions are modelled using linear potential-flow theory, such that the water velocity field is the gradient of a scalar velocity potential $\Phi(x, y, z, t)$. Solutions are sought in the frequency domain, by imposing a time-harmonic condition via

$$\Phi(x, y, z, t) = \mathrm{Re}\left\{\frac{g}{\mathrm{i}\omega}\phi(x, y, z)\,\mathrm{e}^{-\mathrm{i}\omega t}\right\} \quad \text{and} \quad \xi_{i,j}(t) = \mathrm{Re}\left\{\zeta_{i,j}\,\mathrm{e}^{-\mathrm{i}\omega t}\right\} \tag{2.2a,b}$$

for $i \in \{1, 2, \ldots, K\}$ and $j \in \mathbb{Z}$, where $\omega \in \mathbb{R}_+$ is a prescribed angular frequency, $g = 9.81\ \mathrm{m\,s^{-2}}$ is gravitational acceleration, and $\mathrm{i} = \sqrt{-1}$ is the imaginary unit. The (reduced/time-independent) potential $\phi(x, y, z) \in \mathbb{C}$ satisfies Laplace's equation throughout the water domain, i.e.

$$\nabla^2\phi = 0 \quad \text{for} \quad (x, y, z) \in \Omega, \tag{2.3}$$

along with boundary conditions at the seabed and free surface (Mei *et al.* 2005), respectively

$$\partial_z\phi = 0 \quad \text{for} \quad (x, y) \in \mathbb{R}^2 \quad \text{and} \quad z = -h, \tag{2.4}$$

$$\partial_z\phi = \frac{\omega^2}{g}\phi \quad \text{for} \quad (x, y) \in \mathbb{R}^2 \setminus \Gamma \quad \text{and} \quad z = 0. \tag{2.5}$$

It also satisfies conditions on the linearised wetted surfaces of the buoys that equate normal velocities of the water and the buoys, and radiation conditions in the far field,

https://doi.org/10.1017/jfm.2026.12015

$|y| \to \infty$ (defined in § 3.1). The (reduced/time-independent) heave motions $\zeta_{i,j} \in \mathbb{C}$ satisfy equations of motion (defined in § 3.1).

3. Solution method

3.1. *Individual WECs: the diffraction transfer matrix*

Consider an individual WEC (in the absence of surrounding WECs), and suppose that the centre of the WEC in the horizontal plane coincides with the origin, $(x, y) = (0, 0)$. As such, it is convenient to map to cylindrical polar coordinates by writing the velocity potential as $\phi(x, y, z) \equiv \varphi(r, \theta, z)$, where $r > 0$ is the radial coordinate and $\theta \in (-\pi, \pi]$ is the azimuthal coordinate, such that $x = r\cos(\theta)$ and $y = r\sin(\theta)$. The velocity potential is decomposed as

$$\varphi(r, \theta, z) = \varphi^{inc}(r, \theta, z) + \varphi^{scat}(r, \theta, z), \tag{3.1}$$

where φ^{inc} and $\varphi^{scat} \in \mathbb{C}$ are the velocity potentials for the incident and scattered wave fields, respectively. Both velocity potentials satisfy Laplace's equation in the water domain, and the free-surface and seabed boundary conditions (2.3)–(2.5).

The incident wave field φ^{inc} is taken in the general form

$$\varphi^{inc}(r, \theta, z) = \sum_{n=0}^{\infty} \sum_{\mu=-\infty}^{\infty} C_{n\mu}\, I_\mu(\kappa_n\, r)\, \mathrm{e}^{\mathrm{i}\mu\theta}\, Z_n(z), \tag{3.2}$$

where $C_{n\mu} \in \mathbb{C}$ are arbitrary amplitudes, I_μ are modified Bessel functions of the first kind (order μ), and Z_n are the vertical eigenfunctions

$$Z_n(z) = \frac{\cosh(k_n\,(z+h))}{\cosh(k_n\, h)}. \tag{3.3}$$

The wavenumbers k_n are the positive real $(n = 0)$ and the purely imaginary with positive imaginary part $(n \geq 1)$ roots k of the dispersion equation (Mei *et al.* 2005)

$$\omega^2 = gk\tanh(kh). \tag{3.4}$$

To simplify notation, the wavenumbers κ_n are defined for use in the argument of the modified Bessel functions such that $\kappa_n = -\mathrm{i}k_n$ $(n \in \mathbb{Z},\ n \geq 0)$.

The scattered wave field satisfies the Sommerfeld radiation condition

$$\sqrt{r}\left(\partial_r\varphi^{scat} - \mathrm{i}k_0\varphi^{scat}\right) \to 0 \quad \text{as} \quad r \to \infty. \tag{3.5}$$

Thus it can be expressed as (Linton & McIver 2001)

$$\varphi^{scat}(r, \theta, z) = \sum_{n=0}^{\infty} \sum_{\mu=-\infty}^{\infty} D_{n\mu}\, K_\mu(\kappa_n r)\, \mathrm{e}^{\mathrm{i}\mu\theta}\, Z_n(z), \tag{3.6}$$

where $D_{n\mu} \in \mathbb{C}$ are amplitudes to be calculated, and K_μ are modified Bessel functions of the second kind (order μ). The amplitudes $D_{n\mu}$ are decomposed as

$$D_{n\mu} = D_{n\mu}^{diff} + \zeta\, D_{n\mu}^{rad} \quad \text{for} \quad n \in \mathbb{Z},\ n \geq 0, \quad \text{and} \quad \mu \in \mathbb{Z}, \tag{3.7}$$

where $\zeta \in \mathbb{C}$ is the as yet unknown heave amplitude of the buoy for a specified A^{inc}. The amplitudes $D_{n\mu}^{diff}$ are found by solving a diffraction problem in which the buoy is held stationary, and the amplitudes $D_{n\mu}^{rad}$ are found by solving a radiation problem in which the buoy is forced to move with unit amplitude heave motion, without an incident wave field

https://doi.org/10.1017/jfm.2026.12015

(Appendix A). The associated boundary conditions on the wetted surface of the buoy, S_B, are given by, respectively,

$$\frac{\partial \varphi^{diff}}{\partial n} = -\frac{\partial \varphi^{inc}}{\partial n} \quad \text{and} \quad \frac{\partial \varphi^{rad}}{\partial n} = \frac{\omega^2}{g} \quad \text{on} \quad S_B, \tag{3.8}$$

noting that $g/(\mathrm{i}\omega)$ is factored out of ϕ in (2.2*a*).

The heave amplitude ζ is obtained from the equation of motion (Mei *et al.* 2005)

$$\left[-\omega^2(\mathfrak{M} + a(\omega)) - \mathrm{i}\omega\,(b(\omega) + B_{PTO}) + (\mathfrak{C} + C_{PTO})\right]\zeta(\omega) = F^{exc}(\omega). \tag{3.9}$$

On the left-hand side of (3.9), $\mathfrak{M} \equiv \rho\pi L^3$ is the mass of the buoy, and $\mathfrak{C} = \rho g \pi L^2$ is its hydrostatic stiffness, where $\rho = 1025$ kg m^{-3} is the water density. The frequency-dependent coefficients $a(\omega)$ and $b(\omega)$ are the added mass and radiation damping, respectively, which are calculated from the radiation potential φ^{rad} (see § A.2). The coefficients C_{PTO} and B_{PTO} are, respectively, the spring and damping coefficients of the PTO mechanism. The right-hand side of (3.9), $F^{exc}(\omega)$, is the excitation force, which is calculated from the diffraction potential φ^{diff} using the incident amplitudes $C_{n\mu}$ (Appendix A).

A diffraction transfer operator is used to define the relation between the incident amplitudes $C_{n\mu}$ and scattered amplitudes $D_{n\mu}$. Truncating the infinite summations at $n = N_0$ and $\mu = \pm U$ (chosen sufficiently large to achieve a desired level of accuracy) reduces the diffraction transfer operator to a $(N_0 + 1)(2U + 1)$ square matrix $\boldsymbol{B}$ such that

$$\boldsymbol{D} = \boldsymbol{B}\boldsymbol{C}, \tag{3.10}$$

where the entries of the vectors $\boldsymbol{D}$ and $\boldsymbol{C}$ are

$$[\boldsymbol{C}]_{(n-1)\,(2\,U+1)+\mu} = C_{n\mu} \quad \text{and} \quad [\boldsymbol{D}]_{(n-1)\,(2\,U+1)+\mu} = D_{n\mu}, \tag{3.11}$$

for $n = 0, 1, \ldots, N_0$ and $\mu = -U, -U + 1, \ldots, U$. The elements of $\boldsymbol{B}$ are defined in Appendix A.

3.2. *Individual row: plane-wave expansion, scattering matrices and Bloch waves*

Consider an individual row of WECs, in which the WECs are indexed $j \in \mathbb{Z}$, and the horizontal centre of buoy j is located at $(x, y) = (j W_x, 0)$. Each WEC in the row has an associated local polar coordinate system (r_j, θ_j), such that $x = j W_x + r_j \cos(\theta_j)$ and $y = r_j \sin(\theta_j)$. In the local region around WEC j ($r_j < W_x - L$), the velocity potential can be expressed as

$$\phi(x, y, z) = \varphi_j^{inc}(r_j, \theta_j, z) + \varphi_j^{scat}(r_j, \theta_j, z), \tag{3.12}$$

where

$$\varphi_j^{inc}(r_j, \theta_j, z) = \sum_{n=0}^{\infty} \sum_{\mu=-\infty}^{\infty} C_{n\mu}^{j}\, I_\mu(\kappa_n r_j)\, \mathrm{e}^{\mathrm{i}\mu\theta_j}\, Z_n(z) \tag{3.13}$$

and

$$\varphi_j^{scat}(r_j, \theta_j, z) = \sum_{n=0}^{\infty} \sum_{\mu=-\infty}^{\infty} D_{n\mu}^{j}\, K_\mu(\kappa_n r_j)\, \mathrm{e}^{\mathrm{i}\mu\theta_j}\, Z_n(z) \tag{3.14}$$

are the velocity potentials corresponding to the local incident and scattered fields, respectively.

https://doi.org/10.1017/jfm.2026.12015

The row of WECs is excited by an ambient incident wave field, with velocity potential $\phi^{amb}(x, y, z)$. In the local coordinates of WEC j, the velocity potential is expressed as

$$\phi^{amb}(x, y, z) \equiv \varphi_j^{amb}(r_j, \theta_j, z) = \sum_{n=0}^{\infty} \sum_{\mu=-\infty}^{\infty} A_{n\mu}^{j}\, I_\mu(\kappa_n r_j)\, \mathrm{e}^{\mathrm{i}\mu\theta_j}\, Z_n(z), \tag{3.15}$$

where the amplitudes $A_{n\mu}^{j}$ are considered known (i.e. they depend on A^{inc}). The incident wave field for WEC j is expressed as a superposition of the ambient wave field and the scattered wave fields of all other WECs ($l \neq j$) (Kagemoto & Yue 1986), such that the velocity potential of the local incident field is

$$\varphi_j^{inc}(r_j, \theta_j, z) = \varphi_j^{amb}(r_j, \theta_j, z) + \sum_{\substack{l=-\infty \\ l\neq j}}^{\infty} \varphi_{l\to j}^{scat}(r_j, \theta_j, z), \tag{3.16}$$

where $\varphi_{l\to j}^{scat}$ is the velocity potential for the field scattered field by WEC l, expressed in the local coordinates of WEC j. Using Graf's addition theorem (Martin 2006), $\varphi_{l\to j}^{scat}$ has the representation

$$\begin{aligned}\varphi_{l\to j}^{scat}(r_j, \theta_j, z) = \sum_{n=0}^{\infty} \sum_{\mu=-\infty}^{\infty} &\left[\sum_{\tau=-\infty}^{\infty} D_{n\tau}^{l} (-1)^\mu K_{\tau-\mu}(\kappa_n W_{lj})\, \mathrm{e}^{\mathrm{i}(\tau-\mu)\vartheta_{l-j}}\right] \\ &\times I_\mu(\kappa_n r_j)\, \mathrm{e}^{\mathrm{i}\mu\theta_j}\, Z_n(z),\end{aligned} \tag{3.17}$$

where $(r_j, \theta_j) = (W_{lj}, \vartheta_{lj})$ is the origin of the local coordinate system of WEC l in the local coordinates of WEC j, and $r_j < W_{lj}$. Substituting (3.15) and (3.17) into (3.16), and comparing with (3.13), gives

$$C_{n\mu}^{j} = A_{n\mu}^{j} + \sum_{\substack{l=-\infty \\ l\neq j}}^{\infty} \sum_{\tau=-\infty}^{\infty} D_{n\tau}^{l} (-1)^\mu K_{\tau-\mu}(\kappa_n W_{lj})\, \mathrm{e}^{\mathrm{i}(\tau-\mu)\vartheta_{l-j}} \tag{3.18}$$

for $n \in \mathbb{Z}$, $n \geq 0$, $\mu \in \mathbb{Z}$ and $l \in \mathbb{Z}$ (Peter *et al.* 2006).

Suppose that the ambient incident wave field is such that

$$A_{n\mu}^{j} = \mathcal{Q}_j A_{n\mu}, \quad \text{where} \quad \mathcal{Q}_j = \mathrm{e}^{\mathrm{i}k_0 j W_x \cos(\chi)}, \tag{3.19}$$

in which the $A_{n\mu} \equiv A_{n\mu}^{0}$ are known, and $\chi \in (0, \pi)$ denotes the incident angle with respect to the x-axis. (This is the case for a plane ambient incident wave, for example.) Owing to the periodicity of the geometry in the x-direction, $C_{n\mu}^{j}$ and $D_{n\mu}^{j}$ inherit similar quasi-periodic properties, such that

$$C_{n\mu}^{j} = \mathcal{Q}_j\, C_{n\mu} \quad \text{and} \quad D_{\mu}^{j} = \mathcal{Q}_j\, D_{n\mu}, \tag{3.20}$$

where $C_{n\mu} \equiv C_{n\mu}^{0}$ and $D_{n\mu} \equiv D_{n\mu}^{0}$ are to be found. They are intentionally written to match the notation for incident and scattered amplitudes in the individual WEC problem (§ 3.1) to emphasise that they are related by the diffraction transfer matrix, such that $\boldsymbol{D} = \boldsymbol{BC}$.

A relation between the $A_{n\mu}$, $C_{n\mu}$ and $D_{n\mu}$ is found by substituting the quasi-periodicities (3.19)–(3.20) into (3.18), to give

$$C_{n\mu} = A_{n\mu} + \sum_{\tau=-\infty}^{\infty} \sigma_{\tau-\mu}^{n}\, D_{n\tau} \quad \text{for} \quad n \in \mathbb{Z},\ n \geq 0 \quad \text{and} \quad \mu \in \mathbb{Z}, \tag{3.21}$$

https://doi.org/10.1017/jfm.2026.12015

where $\sigma^n_{\tau-\mu}$ is a lattice sum known as a Schlömilch series, defined as

$$\sigma^n_{\tau-\mu} = (-1)^{\mu} \sum_{j=1}^{\infty} \left(\mathcal{Q}_{-j} + (-1)^{\tau-\mu} \, \mathcal{Q}_j \right) \, K_{\tau-\mu}(\kappa_n \, j \, W_x), \tag{3.22}$$

for which an efficient computation method exists (Linton 1998; Peter *et al.* 2006).

Truncating the infinite sums over vertical and Fourier modes, as in § 3.1, (3.21) is expressed as

$$\boldsymbol{C} = \boldsymbol{A} + \boldsymbol{\sigma}\,\boldsymbol{D}, \quad \text{where} \quad [\boldsymbol{A}]_{(n-1)\,(2\,U+1)+\mu} = A_{n\mu}, \tag{3.23}$$

and $\boldsymbol{\sigma}$ is defined in Appendix B. It follows that (Peter *et al.* 2006)

$$\boldsymbol{D} = \boldsymbol{B}(\boldsymbol{A} + \boldsymbol{\sigma}\,\boldsymbol{D}) \quad \Rightarrow \quad \boldsymbol{D} = \left[\boldsymbol{I} - \boldsymbol{B}\boldsymbol{\sigma}\right]^{-1} \boldsymbol{B}\boldsymbol{A}. \tag{3.24}$$

Equation (3.24) gives the local incident amplitudes, and hence the local scattered amplitudes, in terms of the ambient incident amplitudes. The heave amplitude $\zeta \equiv \zeta^0$, which is such that $\zeta^j = \mathcal{Q}_j\,\zeta$, is computed from (3.9) with an exciting force as given in Appendix A.

For $|y| > L$, the wave field can be expressed in terms of a plane-wave expansion (PWE) (Appendix B; Peter & Meylan 2010), such that the velocity potential is

$$\phi(x, y, z) = \sum_{n=0}^{\infty} \sum_{m=-\infty}^{\infty} \Big\{ F^{\pm}_{mn}\, \mathrm{e}^{\mathrm{i}k_n \{x\,\cos(\chi_{mn}) \pm y\,\sin(\chi_{mn})\}} + G^{\mp}_{mn}\, \mathrm{e}^{\mathrm{i}k_n \{x\,\cos(\chi_{mn}) \mp y\,\sin(\chi_{mn})\}} \Big\}\, Z_n(z), \tag{3.25}$$

where $F^{\pm}_{mn}$ and $G^{\pm}_{mn}$ are, respectively, the amplitudes of waves incoming to and outgoing from the row of WECs in the $\pm y$-direction. The χ_{mn} are the scattering angles

$$\chi_{mn} = \arccos\left(\frac{\psi_{mn}}{k_n}\right), \quad \text{where} \quad \psi_{mn} = k_n \cos(\chi) + \frac{2m\pi}{W_x}, \tag{3.26}$$

defined such that $\mathrm{e}^{\mathrm{i}k_n W_x \cos(\chi_{mn})} = \mathrm{e}^{\mathrm{i}k_0 W_x \cos(\chi)}$ for all m and n, and where the complex branch of arccos is defined by (Peter *et al.* 2006)

$$\arccos(\varsigma) = \begin{cases} \mathrm{i}\,\operatorname{arccosh}(\varsigma), & \varsigma > 1, \\ \pi - \mathrm{i}\,\operatorname{arccosh}(-\varsigma) & \varsigma < -1, \end{cases} \tag{3.27}$$

with $\operatorname{arccosh}(\varsigma) = \log(\varsigma + \sqrt{\varsigma^2 - 1})$ for $\varsigma > 1$. There is a finite set

$$\mathcal{M} = \{m \in \mathbb{Z} : |\psi_{m0}| < k_0\} \tag{3.28}$$

such that the scattering angles $\chi_{m0} \in \mathbb{R}$, and thus the corresponding plane waves in (3.25), are propagating. Except for $\chi_{mn} = 0$ or π rad, which correspond to the scattering angle being aligned with the row axis, all other scattering angles are complex-valued ($\chi_{mn} \notin \mathbb{R}$ for $n = 0$ and $m \notin \mathcal{M}$ or $n > 0$), such that they decay exponentially away from the row (those with G-amplitudes) or grow exponentially away from the row (those with F-amplitudes).

The amplitudes of the incoming and outgoing plane waves, $F^{\pm}_{mn}$ and $G^{\pm}_{mn}$, respectively, are related via scattering coefficients R^{ij}_{mn} for reflection and T^{ij}_{mn} for transmission, such

https://doi.org/10.1017/jfm.2026.12015

that

$$G^{\pm}_{ij} = \sum_{n=0}^{\infty} \sum_{m=-\infty}^{\infty} \left\{ R^{ij}_{mn} \, F^{\mp}_{ij} + T^{ij}_{mn} \, F^{\pm}_{ij} \right\} \quad \text{for} \quad j, n \in \mathbb{Z}, \;\; j, n > 0 \quad \text{and} \quad i, m \in \mathbb{Z}, \tag{3.29}$$

where the symmetry of the row with respect to the x-axis has been used. Truncating the infinite summations to $j, n = N_1 \leq N_0$ vertical modes and $M = p + q + 1$ scattering angles ($p, q \geq 0$), such that $i, m = -p, \ldots, q$ can include a finite number of complex scattering angles (N_1, M are sufficient for convergence), the scattering relations (3.29) are expressed in terms of reflection and transmission matrices $\boldsymbol{R}$ and $\boldsymbol{T}$, respectively, such that

$$\begin{pmatrix} \boldsymbol{G}^{-} \\ \boldsymbol{G}^{+} \end{pmatrix} = \begin{bmatrix} \boldsymbol{R} & \boldsymbol{T} \\ \boldsymbol{T} & \boldsymbol{R} \end{bmatrix} \begin{pmatrix} \boldsymbol{F}^{+} \\ \boldsymbol{F}^{-} \end{pmatrix}. \tag{3.30}$$

The vectors $\boldsymbol{F}$ and $\boldsymbol{G}$ have entries

$$[\boldsymbol{F}^{\pm}]_{(m-1)\,(N_1+1)+n} = F^{\pm}_{mn}, \quad [\boldsymbol{G}^{\pm}]_{(m-1)\,(N_1+1)+n} = G^{\pm}_{mn}. \tag{3.31}$$

The entries of the $M \times (N_1 + 1)$ square matrices $\boldsymbol{R}$ and $\boldsymbol{T}$ are given in Appendix B.

Consider the row as existing in a unit cell $\varOmega_{unit}$, where

$$\varOmega_{unit} = \{(x, y, z) \in \varOmega : -W_y/2 < y < W_y/2\}, \tag{3.32}$$

i.e. $\varOmega_{unit}$ is a strip of the water domain of width W_y in the y-direction and with the row of WECs along its centreline. The unit cell has an associated transfer matrix $\boldsymbol{P}$ that maps plane-wave amplitudes from the left-hand side of the unit cell ($y = -W_y/2$) to the right-hand side ($y = W_y/2$), such that (Bennetts & Squire 2009)

$$\begin{pmatrix} \boldsymbol{G}^{+} \\ \boldsymbol{F}^{-} \end{pmatrix} = \boldsymbol{P} \begin{pmatrix} \boldsymbol{F}^{+} \\ \boldsymbol{G}^{-} \end{pmatrix}, \quad \text{where} \quad \boldsymbol{P} = \begin{bmatrix} \boldsymbol{T} - \boldsymbol{R}\boldsymbol{T}^{-1}\boldsymbol{R} & \boldsymbol{R}\boldsymbol{T}^{-1} \\ -\boldsymbol{T}^{-1}\boldsymbol{R} & \boldsymbol{T}^{-1} \end{bmatrix}. \tag{3.33}$$

The eigenspace of the transfer matrix defines the modes supported by the unit cell. In particular, the eigenvalues define wavenumbers $\pm\beta_n$ for the modes, via the relation

$$\operatorname{eig}(\boldsymbol{P}) = \{\exp(\pm \mathrm{i}\beta_n W_y) : n \in \{0, 1, \ldots, M\, N_1\}\}, \tag{3.34}$$

where the $\pm$ pairs indicate the symmetry of the unit cell with respect to the y-axis. The β-wavenumbers and associated modes define so-called Bloch waves supported by the unit cell, which are conventionally considered to exist in the doubly periodic medium that would be formed from repeating the unit cell such that it occupies the entire water domain $\varOmega$ (Chou 1998).

3.3. *Full array: multiple rows*

The PWE associated with row $i \in \{1, 2, \ldots, K\}$ in the array has velocity potential $\phi \equiv \phi_i$, such that

$$\phi_i(x, y_i, z) = \sum_{n=0}^{\infty} \sum_{m=-\infty}^{\infty} \left\{ F^{i\pm}_{mn} \, \mathrm{e}^{\mathrm{i}k_n\{x \cos(\chi_{mn}) \pm y_i \sin(\chi_{mn})\}} + G^{i\mp}_{mn} \, \mathrm{e}^{\mathrm{i}k_n\{x \cos(\chi_{mn}) \mp y_i \sin(\chi_{mn})\}} \right\} Z_n(z), \tag{3.35}$$

where $y_i \equiv y - (i - 1)\, W_y$. Expression (3.35) holds in the strips $L < |y_i| < W_y - L$ that separate row i from the adjacent rows (with suitable modifications for the outermost rows,

https://doi.org/10.1017/jfm.2026.12015

$i = 1$ and K; see below). Upon truncation (at $n = N_1$ and $m = -p, \ldots, q$), the amplitudes $F^{i\pm}_{mn}$ and $G^{i\pm}_{mn}$ are related by reflection and transmission matrices $\boldsymbol{R}_i$ and $\boldsymbol{T}_i$ such that

$$\begin{pmatrix} \boldsymbol{G}_i^- \\ \boldsymbol{G}_i^+ \end{pmatrix} = \begin{bmatrix} \boldsymbol{R}_i & \boldsymbol{T}_i \\ \boldsymbol{T}_i & \boldsymbol{R}_i \end{bmatrix} \begin{pmatrix} \boldsymbol{F}_i^+ \\ \boldsymbol{F}_i^- \end{pmatrix}, \tag{3.36}$$

where the reflection and transmission matrices are evaluated for the PTO parameters applied to row i (in the local coordinates).

A propagating ambient incident field, travelling at angle $\chi \in (0, \pi)$ with respect to the positive x-axis, is prescribed by setting $F^{1+}_{00} = 1$ and $F^{1+}_{mn} = 0$ for n or $m \neq 0$, and $F^{K-}_{mn} = 0$ for all n and m. Reflection and transmission matrices for the entire array, $\mathcal{R}^\pm$ and $\mathcal{T}^\pm$, are used to relate the amplitudes of the ambient incident field (F^{1+}_{mn} and F^{K-}_{mn}) and the amplitudes of the plane waves scattered to the far field (G^{1-}_{mn} to $y \to -\infty$, and G^{K+}_{mn} to $y \to \infty$), such that

$$\begin{pmatrix} \boldsymbol{G}_1^- \\ \boldsymbol{G}_K^+ \end{pmatrix} = \begin{bmatrix} \mathcal{R}^- & \mathcal{T}^- \\ \mathcal{T}^+ & \mathcal{R}^+ \end{bmatrix} \begin{pmatrix} \boldsymbol{F}_1^+ \\ \boldsymbol{F}_K^- \end{pmatrix}, \tag{3.37}$$

where the superscripts $\pm$ are required as the array is not x-symmetric in general (unlike the individual rows).

The reflection and transmission matrices for the array are calculated using a recursive algorithm (Bennetts & Squire 2009; Peter & Meylan 2010) to combine the scattering relations for the individual rows (3.36) for $i \in \{1, 2, \ldots, K\}$ with relations that equate the outgoing plane waves from row i with the incoming waves for row $i + 1$ and vice versa, i.e.

$$\boldsymbol{F}^+_{i+1} = \boldsymbol{Q}\boldsymbol{G}^+_i \quad \text{and} \quad \boldsymbol{Q}^{-1}\boldsymbol{F}^-_i = \boldsymbol{G}^-_{i+1} \quad \text{for} \quad i \in \{1, 2, \ldots, K-1\}, \tag{3.38}$$

where $\boldsymbol{Q}$ is a diagonal phase-change matrix, with entries

$$[\boldsymbol{Q}]_{(m-1)(N_1+1)+n} = \mathrm{e}^{\mathrm{i}k_n W_y \sin(\chi_{mn})}. \tag{3.39}$$

A subsequent recursive algorithm (Bennetts & Squire 2009) is applied to calculate the amplitudes of the wave field between rows $i = 1, 2, \ldots, K$, such that

$$\boldsymbol{F}^+_{i+1} = \left[\boldsymbol{I} - \mathcal{R}^+_{(1,\,i-1)}\boldsymbol{Q}\mathcal{R}^-_{(K,\,i)}\boldsymbol{Q}\right]^{-1}\left[\mathcal{T}^+_{(1,\,i-1)}\boldsymbol{F}^+_1 + \mathcal{R}^+_{(1,\,i-1)}\boldsymbol{Q}\mathcal{T}^-_{(K,\,i)}\boldsymbol{F}^-_K\right], \tag{3.40}$$

$$\boldsymbol{G}^-_{i+1} = \left[\boldsymbol{I} - \mathcal{R}^-_{(K,\,i)}\boldsymbol{Q}\mathcal{R}^+_{(1,\,i-1)}\boldsymbol{Q}\right]^{-1}\left[\mathcal{R}^-_{(K,\,i)}\boldsymbol{Q}\mathcal{T}^+_{(1,\,i-1)}\boldsymbol{F}^+_1 + \mathcal{T}^-_{(K,\,i)}\boldsymbol{F}^-_K\right], \tag{3.41}$$

where $\mathcal{R}^\pm_{(i,\,j)}$ and $\mathcal{T}^\pm_{(i,\,j)}$ denote the combined reflection and transmission matrices, respectively, for rows i to j, with $i, j = 1, 2, \ldots, K$. The amplitude of the zeroth WEC in row i, for $i = 1, 2, \ldots, K$, is retrieved from

$$\zeta_i = \boldsymbol{\zeta}_i\boldsymbol{\sigma}\boldsymbol{D}_i + \boldsymbol{\zeta}_i(\boldsymbol{F}^+_i + \boldsymbol{F}^-_i), \tag{3.42}$$

where the scattered amplitudes for row i are obtained from $\boldsymbol{D}_i = \boldsymbol{B}(\boldsymbol{F}^+_i + \boldsymbol{F}^-_i)$, and $\boldsymbol{\zeta}_i$ is defined in Appendix A.

The proportion of the ambient incident wave field energy absorbed by the array, α, is calculated as

$$\alpha = \sin(\chi) - \sum_{m \in \mathcal{M}} \left(|R_{m0}|^2 + |T_{m0}|^2\right)\sin(\chi_{m0}), \tag{3.43}$$

where R_{m0} and T_{m0} are, respectively, the propagating elements of the reflection and transmission matrices for the array, i.e. α is the proportion of energy not reflected and

https://doi.org/10.1017/jfm.2026.12015

transmitted by the array. In the case where there is no PTO damping ($B_{PTO} = 0$), $\alpha = 0$ and (3.43) reduces to an energy conservation relation (McIver 2000).

4. Numerical results

After specifying the parameters in § 4.1, the framework for grading an array is progressively built in § 4.2. The role of WEC resonances in controlling propagation is established using band structures in § 4.2.1, and linked to the reflection and transmission of the array in § 4.2.2. To create rainbow reflection, the local bandgaps are staggered over the target interval in § 4.2.3, and the resultant reflection and transmission are analysed in complex frequency space to associate the array behaviour with the governing resonant properties. PTO damping is added row-by-row to capture the reflected wave energy for rainbow absorption in § 4.3. The graded design is applied to a finite array in § 4.4, and compared to a uniform tuning in an irregular sea state to demonstrate practical relevance.

4.1. *Parameter ranges and implications*

The water depth is set to $h = 50$ m, and the WEC diameter is fixed as $2L = 10$ m to resemble the parameter regime of the CorPower Ocean (2026) C4 device. The WEC separations, W_x and W_y, are such that the distance between the nearest points of adjacent buoys is between 1.5 and 3 times the WEC diameter, similarly to Sharp & DuPont (2018). The PTO spring constants are set to achieve WEC resonances over the target range $\omega \in [0.3, 0.65]$ rad s^{-1} ($\approx$ 9.6–20.9 s wave periods), which requires negative stiffness values in (A21), as successfully demonstrated for the C4 WEC (Todalshaug *et al.* 2016). The PTO damping is unrestricted, and values are chosen to capture large proportions of incident wave energy (see § 4.3).

The incident wavelengths over the frequency range of interest ($\omega \in [0.3, 0.65]$ rad s^{-1}) are $\lambda \approx 142-428$ m. Incident directions are considered in the range $\pi/6 \le \chi \le \pi/2$ (where $\chi = \pi/2$ rad is normal incidence), which is equivalent to $\pi/2 \le \chi \le 5\pi/6$ by symmetry. The incident amplitude is arbitrary, as a linear model is used. As $\lambda/2 > W_x$ for $\omega \in [0.3, 0.65]$ rad s^{-1}, there is a single propagating scattering angle (the incident wave direction χ, so that $\mathcal{M} = \{0\}$) over the frequency range of interest (Falnes & Budal 1982). Additional scattering angles cut-on, e.g. at $\omega \approx 1.43$ rad s^{-1} for normal incidence ($\chi = \pi/2$ rad), and at $\omega \approx 1.03$ rad s^{-1} for $\chi = \pi/8$ rad when $W_x = 30$ m. Complex scattering angles are included in calculations to capture resonant interactions between rows accurately. Where ambiguity is unlikely, the reflection and transmission coefficients of the sole propagating mode (see (3.43)) are denoted $|R|^2$ and $|T|^2$, respectively.

There is a maximum of one propagating Bloch wave over the frequency range of interest, associated with the Bloch wavenumber that tends to $k_0 \sin(\chi)$ at low frequencies, which is designated $\beta \equiv \beta_0$. For a given unit cell, its passbands are the frequency intervals on which the Bloch wavenumber is real-valued, $\beta_0 \in \mathbb{R}_+$, i.e. the unit cell supports the propagation of the Bloch wave for the passband frequencies. Bandgaps are the frequency intervals on which the Bloch wavenumber is complex-valued, $\beta_0 \in \mathbb{R}_+ + \mathrm{i}\,\mathbb{R}_+$, i.e. the Bloch wave decays across the unit cell for bandgap frequencies. As $\lambda > 2W_y \ge 2W_y \sin(\chi)$ for $\omega \in [0.3, 0.65]$ rad s^{-1}, bandgaps are achieved on the target frequency interval via local resonance only. Bragg bandgaps (centred around $k_0 = \pi/(W_y \sin(\chi))$) occur at higher frequencies, e.g. for $\omega \in (0.85, 0.95)$ rad s^{-1} at normal incidence ($\chi = \pi/2$ rad) when $W_x = 30$ m and $W_y = 40$ m (figure 2).

https://doi.org/10.1017/jfm.2026.12015

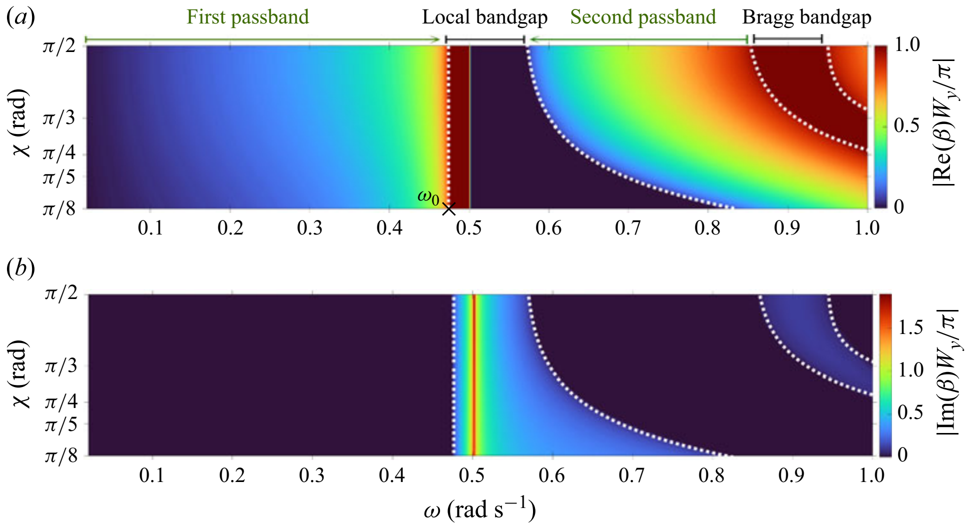

Figure 2. Dispersion curves (as surface plots) of the (*a*) real and (*b*) imaginary parts of the Bloch wavenumber for a row of WECs tuned to $\omega_0 = 0.475$ rad s^{-1} (marked with a cross in (*a*)), for incident angles χ between $\pi/8$ and $\pi/2$, when $W_x = 30$ m and $W_y = 40$ m.

4.2. *Preliminary results*

4.2.1. *Band structures for individual rows*

Figure 2 shows a surface plot (dispersion diagram) of the real and imaginary parts of the Bloch wavenumber for a row of WECs tuned to $\omega_0 = 0.475$ rad s^{-1} (the middle of the target frequency range) using (A21), for incident angles between $\chi = \pi/8$ rad (near grazing incidence) and $\chi = \pi/2$ rad (normal incidence). For all incident angles, a passband ($\mathrm{Im}(\beta) = 0$) exists at low frequencies, such that the Bloch wave propagates across the unit cell. A local bandgap begins close to the resonant frequency ω_0 for all incident angles. In the low-frequency part of the local bandgap, $\mathrm{Re}(\beta\, W_y) = \pi$, whilst $\mathrm{Im}(\beta\, W_y)$ increases monotonically and unboundedly, up to $\omega \approx 0.5$ rad s^{-1} for all incident angles.

As the frequency increases above $\omega \approx 0.5$ rad s^{-1}, the Bloch wavenumber switches to a branch where $\mathrm{Re}(\beta\, W_y) = 0$ and $\mathrm{Im}(\beta\, W_y)$ decreases monotonically (the corresponding eigenvalue of the transfer matrix moves from the negative real axis to the positive real axis). This marks a transition from a 'locally resonant' regime where resonances of the individual WECs dominate, to a Bragg regime where the wavelength across the unit cell dominates. Hence the incident angle has a greater influence over the band surface, but at different rates for the different incident angles, such that $\mathrm{Im}(\beta\, W_y)$ reaches zero (the transition to the second passband) at higher frequencies as the incident angle decreases (away from normal incidence), thus widening the local bandgaps.

Similarly, the second passband widens at an increasing rate as the incident angle decreases. The Bragg bandgap determines the upper bound of the second passband, and moves up in frequency as the incident angle decreases. In the Bragg bandgap, $\mathrm{Re}(\beta\, W_y) = \pi$ and $\mathrm{Im}(\beta\, W_y)$ increases monotonically up to the centre of the bandgap, before monotonically decreasing to $\mathrm{Im}(\beta\, W_y) = 0$. The band structures in figure 2 are representative of the behaviour for all resonant frequencies lying within the target interval ($\omega_0 \in [0.3, 0.65]$ rad s^{-1}). The location of the local bandgap shifts up or down depending on the resonant frequency, which extends or contracts the second passband accordingly.

https://doi.org/10.1017/jfm.2026.12015

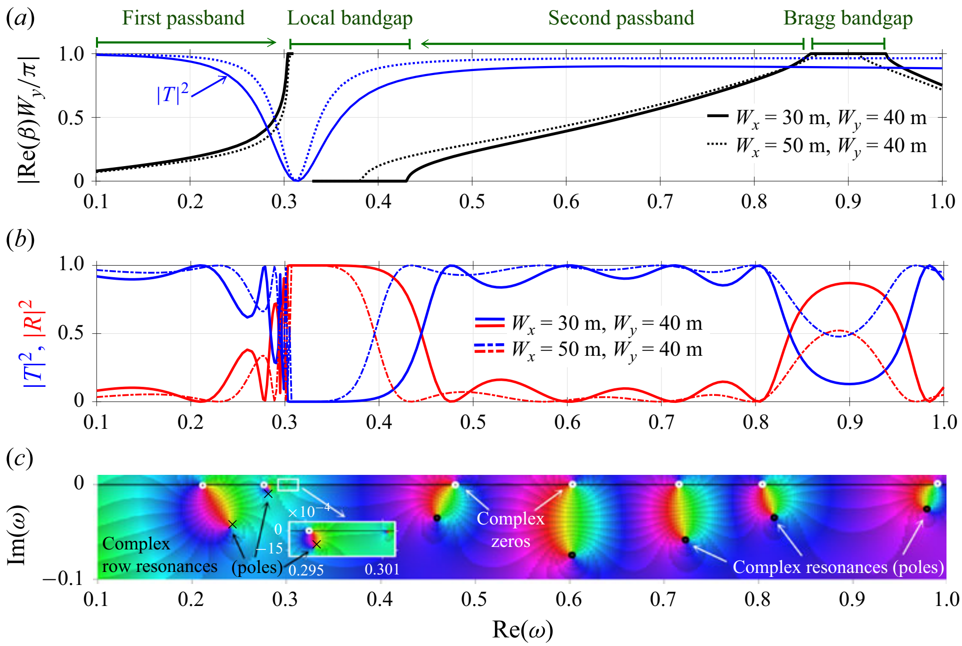

Figure 3. (a) Dispersion curves (black lines) and transmission $|T|^2$ (blue lines) for a row of WECs tuned to $\omega_0 = 0.3$ rad s^{-1} with $W_x = 30$ m (solid lines) and $W_x = 50$ m (dotted lines) at $\chi = \pi/2$ rad with $W_y = 40$ m. (b) Transmission $|T|^2$ and reflection $|R|^2$ (red lines) for a uniform array of five rows, where $|T|^2 \approx 0$ and $|R|^2 \approx 1$ in the local bandgaps. (c) Phase portrait of the reflection coefficient $R(\omega)$ when $W_x = 30$ m. The hue represents the magnitude of the colour-coded phase $\arg(R)$, and poles/zeros are identified by rapid phase changes (Wegert 2012).

4.2.2. *Broadband reflection by non-absorbing uniform arrays*

The reflection $|R|^2$ properties of a uniform, non-absorbing array (and also the transmission $|T|^2 = 1 - |R|^2$) are directly connected to the band structures for a unit cell. The relationship is illustrated in figure 3 using normally incident waves to an array of five rows, where all rows are tuned to $\omega_0 = 0.3$ rad s^{-1}. Passbands permit propagation through the array, resulting in oscillatory reflection and transmission coefficients due to wave interference along the array. Bandgaps prevent propagation through the array, generating high reflection and low transmission through destructive interference.

The width of the local bandgap is influenced by the choice of in-row spacing, W_x, as shown in figure 3(a). Smaller W_x-values produce stronger reflection/scattering, which widens the local bandgap and the resonance bandwidth of individual rows, and leads to higher reflection in the Bragg bandgap (figure 3b). Compared to a one-dimensional (1-D) array (Westcott *et al.* 2024), rows of WECs have narrower resonance bandwidths and are weaker reflectors, particularly as W_x increases relative to the WEC diameter (Bennetts & Squire 2009), i.e. $(W_x - 2L) \rightarrow 0$ increases similarity to a 1-D array.

The reflection and transmission in the second passband are governed by array resonances that arise from interference between waves reflected back and forth between the rows in the y-direction (i.e. do not exist for a single row). These manifest as pole–zero pairs in the complex plane, and are shown using the phase portrait (Wegert 2012) of the reflection coefficient as a function of $\omega \in \mathbb{C}$ in figure 3(c). The pole–zero pairs generate zeros in reflection and peaks in transmission for $\omega \in \mathbb{R}$ (figure 3b). The distance between the pole and zero in a given pair determines the associated resonance bandwidth (Romero-García *et al.* 2016).

https://doi.org/10.1017/jfm.2026.12015

Row i	1	2	3	4	5
ω_0^i rad s^{-1}	0.617	0.500	0.410	0.324	0.296
C_{PTO}^i kN m^{-1}	−533	−618	−674	−717	−729
B_{PTO}^i kN s m^{-1}	111	60.3	48.3	30.2	11.1

Table 1. Resonant frequency ω_0, and PTO parameters C_{PTO} and B_{PTO}, for each row in the graded array of five rows with $W_x = W_y = 25$ m used for the results in figure 6.

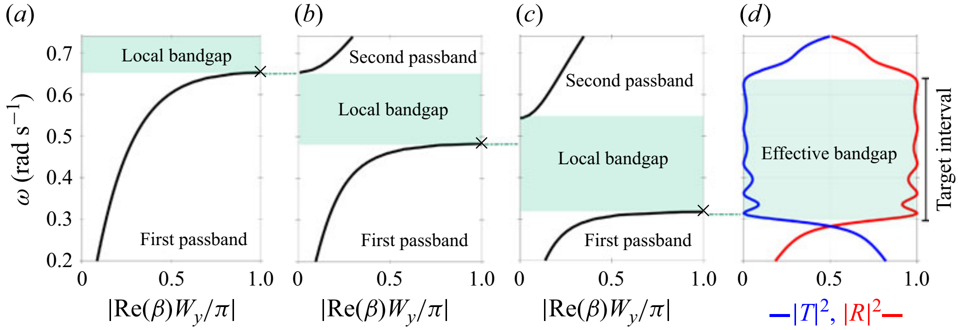

Figure 4. Band diagrams for rows of WECs tuned to (*a*) $\omega_0 = 0.65$ rad s^{-1}, (*b*) $\omega_0 = 0.475$ rad s^{-1} and (*c*) $\omega_0 = 0.31$ rad s^{-1}, with $W_x = W_y = 25$ m and $\chi = \pi/2$ rad. Resonances (marked with crosses) induce local bandgaps (shaded green). A graded array of five rows, in which (*a–c*) are the first, third and fifth rows, creates (*d*) an effective bandgap on $\omega \in [0.3, 0.65]$ rad s^{-1}, such that $|T|^2 \approx 0$ and $|R|^2 \approx 1$.

The locations of the array resonances are determined by the resonant properties of the rows and the row spacing, W_y. Strongly reflective rows have a greater ability to move array resonances up in frequency, reducing the width of the second passband. For example, decreasing $W_x = 50$ m to $W_x = 30$ m shifts the start of the second passband from $\omega = 0.38$ rad s^{-1} to $\omega = 0.43$ rad s^{-1} (figure 3*a*). The Bragg bandgap moves up in frequency as W_y decreases, with $W_y \leq 50$ m required to keep the Bragg bandgap sufficiently far above the target interval to prevent strong interference between row and array resonances.

4.2.3. *Rainbow reflection for non-absorbing graded arrays*

Rainbow reflection is generated by grading the resonant frequencies of the K rows via the PTO springs from high to low ($\omega \approx 0.65 \rightarrow \omega \approx 0.3$ rad s^{-1}) in the y-direction, such that the resonance of row i lies in the local bandgap of row $i+1$. Figures 4(*a–c*) show the band diagrams for rows $i = 1, 3, 5$ in a graded array of $K = 5$ rows at normal incidence, for the PTO spring constants given in table 1 ($B_{PTO}^i = 0$ for $i = 1, 2, \ldots, 5$). Spacings at the lower end of the considered interval, $W_x = W_y = 25$ m, are used to push the second passband to relatively high frequencies, which gives the clearest demonstration of the approach used to create rainbow reflection. Overlapping of local bandgaps on the corresponding unit cells associated with adjacent rows creates a wide effective bandgap for the graded array over $\omega \in [0.3, 0.65]$ rad s^{-1}, where $|T|^2 \approx 0$ and $|R|^2 \approx 1$ (figure 4*d*).

Qualitatively, the band structures are identical to the 2-D case (see figure 5 of Westcott *et al.* 2024). However, the grading of PTO parameters depends on the resonant properties and chosen spacing in three dimensions, which differ substantially from the 2-D model. In particular, less gradual gradings are required in two dimensions as the WECs are

https://doi.org/10.1017/jfm.2026.12015

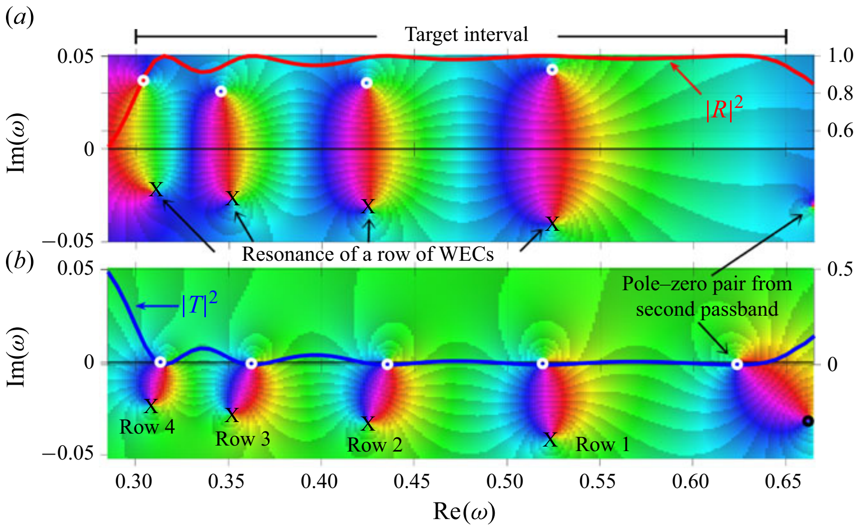

Figure 5. Phase portraits of (*a*) the reflection coefficient $R(\omega)$, and (*b*) the transmission coefficient $T(\omega)$, of the rainbow reflecting array (figure 4, table 1) are shown as functions of complex frequency ($\omega \in \mathbb{C}$), with $|R|^2$ and $|T|^2$ for $\omega \in \mathbb{R}$ overlaid when $B^i_{PTO} = 0$ for $i = 1, 2, \ldots, 5$. The resonance (pole) associated with each row of WECs is marked with a cross, and zeros are depicted by circles. The pole–zero pair for row 5 lies below the axes limits.

strongly reflecting (Westcott *et al.* 2024). However, the grading must force the resonances apart in frequency to reduce strong hydrodynamic interactions, in order to control the resonant properties for low transmission over the target interval, which requires a close spacing to prevent the second passband from constraining the target interval (Westcott *et al.* 2024). In contrast, rows are relatively weak reflectors and require a gradual grading for low transmission in three dimensions. The radiated wave field of each WEC in a row decays with distance in three dimensions, so that a larger W_x is associated with weaker hydrodynamic interactions, and reduces the strength of reflection.

The zeros in transmission and associated peaks in reflection of the graded array over the target interval (figure 4*d*) are governed by pole–zero pairs in complex frequency space (figure 5). Poles correspond to the resonances of the rows, and are located in the lower half of the complex plane. The associated zeros in reflection are displaced from the real frequency axis (figure 5*a*), while zeros in transmission lie on $\mathrm{Im}(\omega) = 0$ (figure 5*b*), and are staggered across the target interval at locations associated with the local bandgaps on the corresponding unit cells. The exception is the $|T|^2 \approx 0$ and $|R|^2 \approx 1$ case at $\omega \approx 0.62$ rad s^{-1}, which is governed by a pole–zero pair that corresponds to a resonance along the second passband, i.e. it is generated by de-coherence between the Bloch waves produced by reflections and re-reflections at the ends of the array.

To maintain low transmission over the target interval ($<1\,\%$ of the incident energy), the grading is such that the resonant frequencies of rows are relatively close together at low frequencies, where rows have narrower resonance bandwidths, and are located farther apart as the resonance bandwidths broaden at higher frequencies. The pole that originates from the second passband (at $\omega \approx 0.66 - 0.03\mathrm{i}$ rad s^{-1} in figure 5, noting that the pole in reflection is not marked for clarity) restricts how high up the target frequency interval the local bandgap can be extended, as interference between the poles created by the second passband and the row resonances down-shift the row resonances in frequency. However, weaker multiple scattering interactions in three dimensions (which decay with distance)

https://doi.org/10.1017/jfm.2026.12015

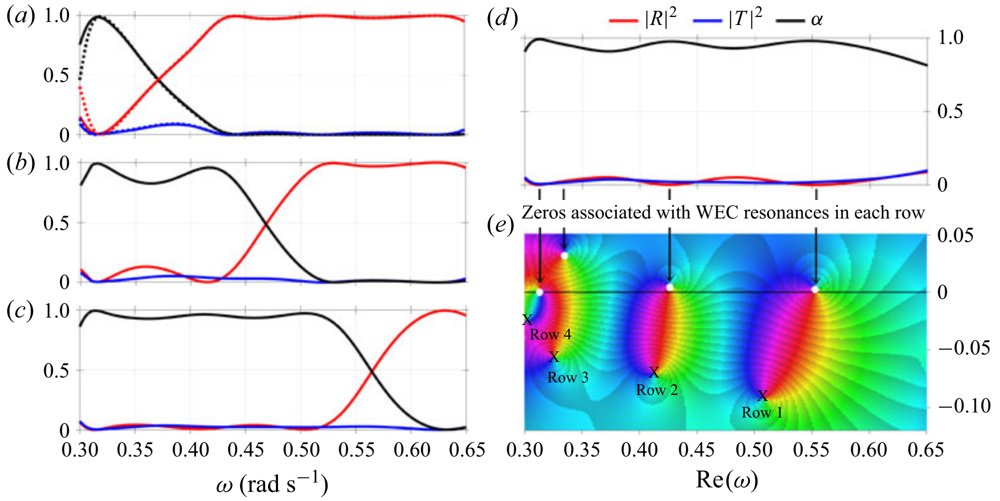

Figure 6. The PTO damping for the (*a*) fifth and fourth, (*b*) third, (*c*) second and (*d*) first row in a graded array of five rows (table 1) is successively chosen to create zeros in reflection $|R|^2$ (red), producing peaks in absorption α (black). Dotted lines in (*a*) give the α, $|R|^2$ and transmission $|T|^2$ (blue) when only $B^4_{PTO} \neq 0$. Each $|R(\omega)|^2 \approx 0$, $\omega \in \mathbb{R}$, translates zeros in the complex plane towards $\mathrm{Im}(\omega) \approx 0$, which are shown in (*e*) the phase portrait of the reflection coefficient $R(\omega)$, for $\omega \in \mathbb{C}$. The zero for row 3 is displaced from $\mathrm{Im}(\omega) \approx 0$.

compared to two dimensions (e.g. see Westcott *et al.* 2024) produce less interference at the upper bound of the target interval, and permit wider spacings between rows. For a fixed spacing in the y-direction, such that $W_y \leq 50$ m, the minimum number of rows required to achieve an effective bandgap over the target interval depends on W_x owing to the associated transmission properties (§ 4.2.2).

4.3. *Broadband absorption*

In graded arrays, wave energy is selectively slowed according to frequency as the group velocity of the associated Bloch wave decreases to zero, and the incident wave energy is amplified near the row with a comparable resonant frequency, which defines the transition to a local bandgap (not shown here, but see e.g. Bennetts *et al.* 2019). In a rainbow reflecting array, the incident energy is subsequently reflected out of the array. Rainbow absorption is created by extracting the amplified energy in the array before it is reflected.

In the WEC array context, PTO dampers are used to extract the incident wave energy. For the graded array of five rows (figure 5), the PTO damping (table 1) is chosen to create near-zeros in reflection and corresponding peaks in absorption, starting with the penultimate row and working towards the front of the array (low-to-high frequency; figures 6*a–d*). The fourth row is less able to sustain low reflection as a result of a narrow resonance bandwidth, which causes a rapid rise in reflection around $\omega = 0.3$ rad s^{-1}. To counteract this, relatively low damping (compared to other rows) is applied to the fifth row (in contrast to the 2-D case where no damping was applied to the final WEC; Westcott *et al.* 2024) to reduce reflection and achieve $|R|^2 \approx |T|^2 \approx 0$ in combination with the fourth row at $\omega \approx 0.3$ rad s^{-1}.

Near-zeros in reflection for real frequencies translate the complex zeros of reflection associated with row resonances towards $\mathrm{Im}(\omega) = 0$ in the complex frequency plane (figure 6*e*). The complex zero associated with row 3 is displaced from $\mathrm{Im}(\omega) \approx 0$ due to interactions between closely spaced pole–zero pairs in frequency space that result

https://doi.org/10.1017/jfm.2026.12015

Row i	1	2	3	4	5	6
ω_0^i rad s^{-1}	0.611	0.567	0.511	0.418	0.342	0.3
C_{PTO}^i kN m^{-1}	−538	−572	−611	−670	−709	−728
B_{PTO}^i kN sm^{-1}	111	52.3	60.3	56.3	40.2	13.7

Table 2. The resonant frequency ω_0 and PTO parameters of each row in the graded array of six rows with $W_x = 30$ m and $W_y = 40$ m.

from the gradual grading of row resonances required to maintain low transmission and reflection at low frequencies. Reflection and transmission rise at the upper bound of the target interval ($|R|^2 < 0.089$ and $|T|^2 < 0.099$ on $\omega \in [0.3, 0.65]$ rad s^{-1}) as a result of interference between the row and array resonances (a pole–zero pair from the second passband is located at $\omega = 0.66$ rad s^{-1}), which limits control over the location of pole–zero pairs through the PTO parameters (Westcott *et al.* 2024). Consequently, relatively high damping is required for row 1 compared to rows 2–5 to maintain low reflection at the upper bound of the target interval.

A good combination of high absorption and a modest number of rows, using practical WEC spacings, is obtained by grading an array of six rows when $W_x = 30$ m and $W_y = 40$ m with the PTO parameters in table 2. The graded array maintains $|T|^2 < 0.085$ and $|R|^2 < 0.078$ on $\omega \in [0.3, 0.65]$ rad s^{-1}, and has average absorption

$$\hat{\alpha} \equiv \frac{1}{0.35} \int_{0.3 \text{ rad s}^{-1}}^{0.65 \text{ rad s}^{-1}} \alpha \, \mathrm{d}\omega = 0.9489, \tag{4.1}$$

i.e. $\approx 95\,\%$ of the incident wave energy is captured at normal incidence ($\chi = \pi/2$ rad). The efficient broadband absorption at normal incidence is maintained over a wide range of incident wave directions (see below), as the row resonances, which control the local band structures, are unaffected by the incident wave angle.

Figure 7 illustrates how the resonances of rows control the spatial separation, and subsequent capture, of incident frequencies at three different incident angles. The frequencies $\omega = 0.52, 0.43, 0.35$ rad s^{-1}, which slightly exceed the resonant frequencies of rows 3, 4 and 5, respectively (i.e. they lie in the associated bandgap), are chosen to demonstrate how the local band structures associated with the corresponding unit cell control propagation. Incident waves propagate until reaching the spatial location in the array at which the resonance of the row on the associated unit cell is lower than the incident frequency, resulting in an abrupt and substantial decrease in transmission. The WEC motions are amplified at these locations, due to the accumulation of incident energy, which is captured by the PTO damping in the rainbow absorbing array.

The absorption of the graded array of six rows over the target interval is shown in figure 8(*a*), for incident angles from normal ($\chi = \pi/2$ rad) to near grazing ($\chi = \pi/6$ rad). As the incident angle decreases, transmission (figure 8*b*) decreases over the target interval (local bandgaps widen in frequency space and increasingly overlap), causing absorption to increase across the target interval, with the average absorption peaking at $\hat{\alpha} \approx 0.955$ when $\chi \approx \pi/3$ rad. However, near-zeros in reflection are gradually lost as χ decreases past $\chi \approx \pi/3$ rad (figure 8*c*), causing absorption to decline on the upper half of the target interval and between the peaks in absorption associated with near-zeros of reflection.

The initial increase in absorption, followed by a gradual decline as the incident wave angle decreases, is observed at different combinations of W_x and W_y, and is particularly noticeable for $W_x = W_y = 50$ m (figure 9). Since larger in-row separations (e.g. $W_x = 50$ m

https://doi.org/10.1017/jfm.2026.12015

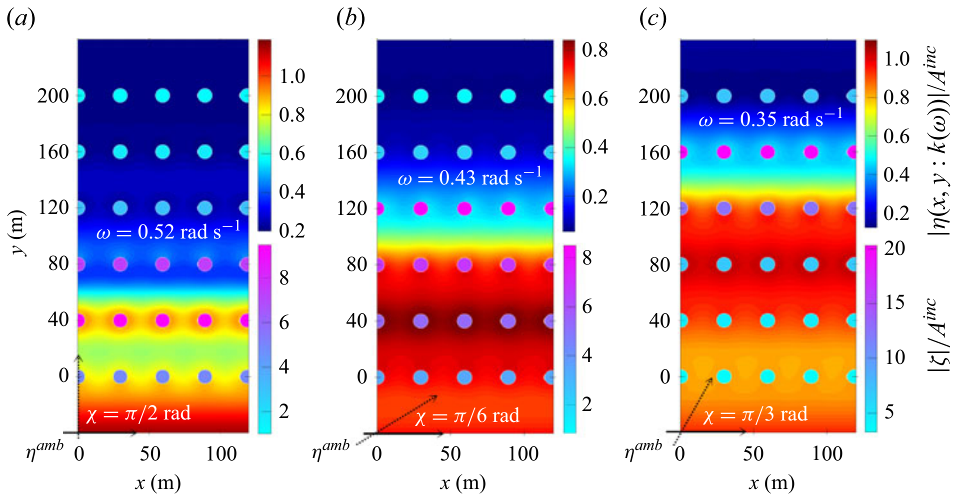

Figure 7. Moduli of the non-dimensionalised surface elevation (upper colour bars) and WEC amplitudes (lower colour bars) in a graded array of six rows (table 2) for frequencies and incident angles (*a*) $\omega = 0.52$ rad s^{-1} and $\chi = \pi/2$ rad, (*b*) $\omega = 0.43$ rad s^{-1} and $\chi = \pi/6$ rad, and (*c*) $\omega = 0.35$ rad s^{-1} and $\chi = \pi/3$ rad. (Note that the coordinate axes are rotated by 90° in the anticlockwise direction compared to figure 1.)

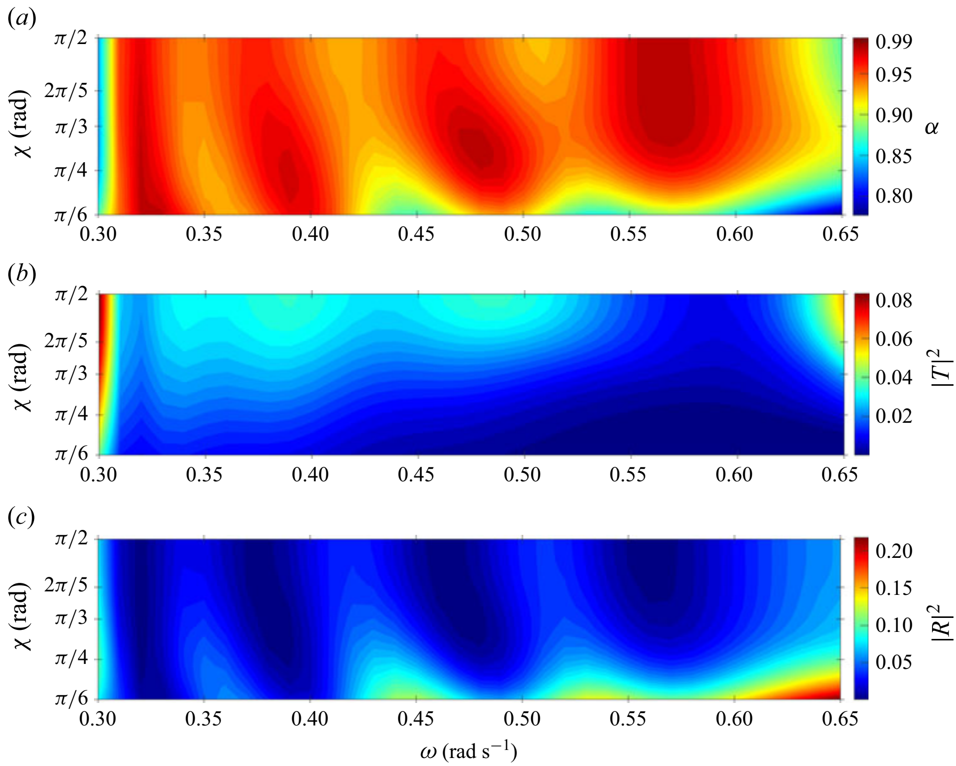

Figure 8. (*a*) Absorption, (*b*) transmission and (*c*) reflection of an array of six rows ($W_x = 30$ m and $W_y = 40$ m; table 2) versus frequency $\omega \in [0.3, 0.65]$ rad s^{-1} and incident angle $\chi \in [\pi/6, \pi/2]$ rad.

https://doi.org/10.1017/jfm.2026.12015

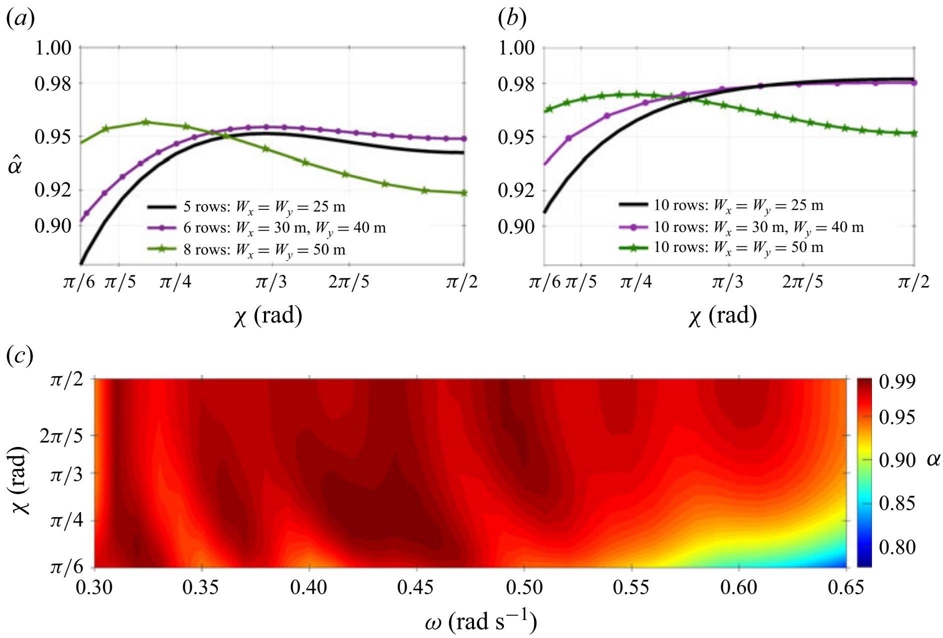

Figure 9. (a,b) Average absorptions versus the incident wave angle for: (a) $K = 5$, 6 and 8 rows, and different choices of W_x and W_y; and (b) $K = 10$ rows, and different choices of W_x and W_y. (c) Absorption of an array of ten rows with $W_x = 30$ m and $W_y = 40$ m versus frequency and incident angle.

versus $W_x = 30$ m) support greater transmission, the reduction in transmission as the incident angle decreases from $\chi = \pi/2$ rad to $\chi = \pi/6$ rad outweighs the gradual displacement of near-zeros in reflection, and results in higher absorption at $\chi = \pi/6$ rad compared to $\chi = \pi/2$ rad. A greater number of rows counteracts this trend (figure 9b), provided that there are sufficiently many rows to create low transmission over the target interval at normal incidence, such that absorption monotonically declines as the incident angle decreases. The various array layouts maintain high absorption for $\pi/6 \leq \chi \leq 5\pi/6$ (by symmetry, $\pi/2 \leq \chi \leq 5\pi/6$ produces equivalent α to figure 9), with the average absorption $\hat{\alpha} > 90\,\%$ for all but the case with five rows (where $\hat{\alpha} = 0.878$ at $\chi = \pi/6$ rad).

For fixed W_x and W_y, the average absorption increases with the number of rows (figure 9(a) versus figure 9(b)). The average absorption of the graded array of ten rows, with spacings $W_x = 30$ m and $W_y = 40$ m, reaches 98 % at normal incidence (figure 9, $\chi = \pi/2$ rad), noting that an optimisation algorithm has not been applied. The slightly lower absorption than obtained for ten WECs in two dimensions (over 99 %; Westcott *et al.* 2024) is attributed to rows of WECs being weaker reflectors than 2-D WECs. Absorption by the ten rows exceeds 95 % over the majority of the target frequency interval and incident angles considered (figure 9c).

4.4. *Finite arrays*

Strategies for broadband absorption extend effectively to arrays in which each row contains a finite number J of WECs (Appendix C). The non-dimensionalised WEC amplitudes (relative to the incident amplitude) in a finite array of 60 WECs (($K = 6$ rows) $\times$ ($J = 10$ WECs per row)) are shown in figure 10, although the rainbow absorption behaviour of graded infinite arrays can be replicated with as few as $J = 5$ WECs per row (not shown). The rows are graded using the PTO parameters in table 2, with $W_x = 30$ m and $W_y = 40$ m.

https://doi.org/10.1017/jfm.2026.12015

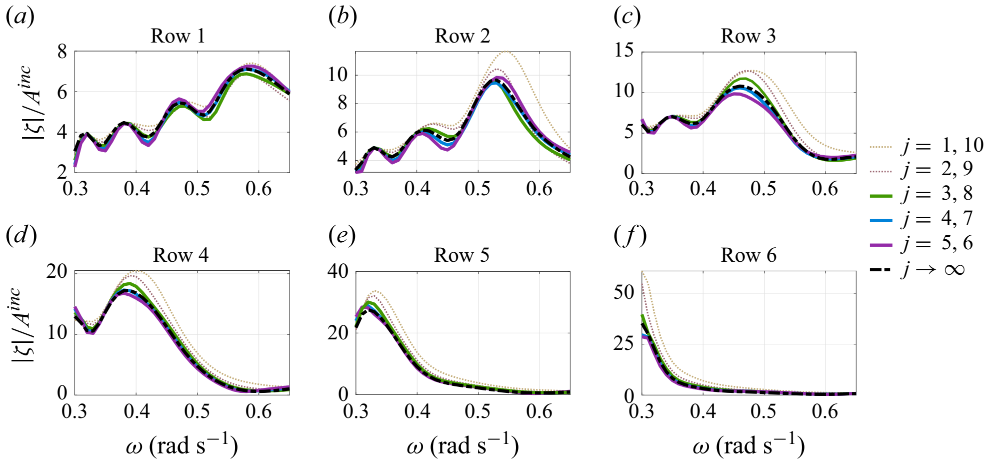

Figure 10. Non-dimensional WEC amplitudes ($|\zeta|/A^{inc}$) in a graded array of 60 WECs with $W_x = 30$ and $W_y = 40$ m for $\omega \in [0.3, 0.65]$ rad s^{-1} at normal incidence ($\chi = \pi/2$ rad). The PTO parameters of the infinite row i in table 2 ($|\zeta|/A^{inc}$, dashed black) are applied to all WECs (numbered 1–10 from left to right) in row i of the finite array, with $i = 1, 2, \ldots, 6$. Interior WECs (solid lines) are numbered $j = 3$–8, and boundary WECs (light coloured dotted lines) by $j = 1, 2, 9, 10$.

The finite array has boundary effects, which are observed in the responses of the WECs at the ends of the rows (WECs at $j = 1$–2 and $(J-1)$–J). These are most prominent near resonance, where the boundary WECs experience amplified motions compared to the corresponding infinite array. The amplitudes of interior WECs $j = 3$–8 closely resemble the WEC amplitudes in the infinite array. Increasingly many interior WECs resemble the behaviour of the infinite array as the number of WECs per row increases.

To evaluate the absorption performance of finite arrays, a relative capture width CW_{finite} is defined as the power captured by the array as a proportion of the power available in the wavefront across the width of the array (JW_x) (McIver 1994; He *et al.* 2022; Gong *et al.* 2024), such that

$$CW_{finite} = \left[\frac{1}{2}\sum_{i=1}^{K}\sum_{j=1}^{J} B_{PTO}^{i}\,\omega^2\,|\zeta_{i,j}|^2\right] \Big/ \left[\frac{\omega}{4k_0}\left(1 + \frac{2k_0h}{\sinh(2k_0h)}\right)|A^{inc}|^2\,JW_x\right]. \tag{4.2}$$

Since the relative capture width is non-dimensionalised relative to the array's cross-sectional width (including $W_x/2$ on either side), the efficiency measure can exceed 1 as the finite array can capture energy from the sides of the array, unlike the infinite array, where $0 \leq \alpha \leq 1$. Efficiencies exceeding 1 are primarily attributed to boundary effects in the finite array, where the resulting amplification of WEC motions increases the numerator in (4.2). At normal incidence, the boundary effects are generally limited to 2–3 edge WECs (either side of the array). Consequently, the proportion of power capture attributed to edge effects gradually decreases as the number of WECs per row increases.

Figure 11(*a*) shows the relative capture width of the finite array of 60 WECs (figure 10), including when the two WECs at the edges of each row that experience boundary effects are removed, such that the second summation in (4.2) runs from $j = 3$ to $(J-2)$, and the capture width is $(J-4)W_x$. The locations of peaks in the relative capture width are consistent with the absorption of the infinite array, but vary in magnitude over the target interval. Correspondence to the infinite array improves as the number of WECs per row increases, and is particularly good when based on the behaviour of interior WECs. For

https://doi.org/10.1017/jfm.2026.12015

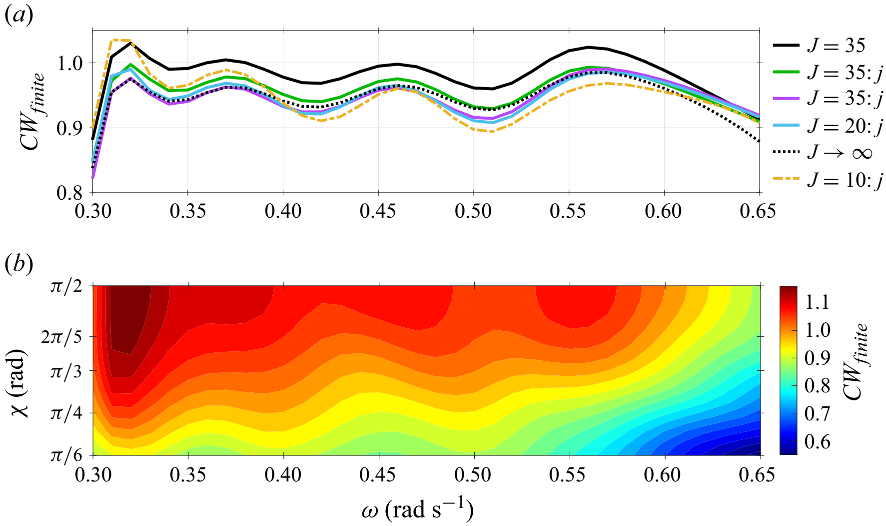

Figure 11. (*a*) Relative capture widths of graded, finite arrays (table 2) versus frequency, with the absorption of the corresponding infinite array overlaid, and including when the boundary WECs ($j = 1, 2, J - 1, J$) are removed. (*b*) Relative capture width of the graded array of 60 WECs (figure 10, table 2) versus frequency and incident angle.

example, the relative capture width for $J = 35$ WECs per row is qualitatively identical to the infinite array, but with higher efficiency, which tends towards the absorption of the infinite array as edge WECs are excluded. There is little change in the relative capture width of interior WECs beyond $J = 20$ WECs per row.

Like the infinite array, the relative capture width of the graded array of 60 WECs remains high over the target interval $\omega \in [0.3, 0.65]$ rad s^{-1} at normal incidence, and gradually decreases as $\chi \to \pi/6$, particularly at higher frequencies (figure 11*b*). The finite array preserves the underlying band structures, which are robust to changes in the incident wave direction, despite boundary effects impacting an increasing number of WECs within each row as the incident angle decreases. For incident angles $\chi \in [\pi/6, \pi/2]$ rad, the finite array achieves over 90 % efficiency on the majority of the target interval (figure 11*b*).

The non-dimensionalised surface elevation and WEC amplitudes for the array of 60 WECs are shown in figure 12, where the frequencies and incident angles correspond to two of the cases used for the infinite array in figure 7. Boundary effects are evident near resonance, and have a reasonably minor impact on the wave field. The finite array permits slightly higher transmission across the width of the array, particularly as $\chi \to \pi/6$. For example, the non-dimensional surface elevation in the finite array is $|\eta(x, y : k)|/A^{inc} \approx 0.23$ when $\omega = 0.52$ rad s^{-1} at $\chi = \pi/2$ rad, and $0.17 \leq |\eta(x, y : k)|/A^{inc} \leq 0.25$ when $\omega = 0.35$ rad s^{-1} at $\chi = \pi/3$ rad, for $-75 < x < 75$ m and at $y = 220$ m, compared to $|\eta(x, y : k)|/A^{inc} \approx 0.17$ and $|\eta(x, y : k)|/A^{inc} \approx 0.14$, respectively, in the infinite array.

4.4.1. *Ocean wave spectra*

To illustrate the broadband (frequency and direction) efficiency of the graded finite array, consider a multi-directional, irregular sea state defined by the wave energy density

$$S(\omega, \theta) = S_f(\omega)\, D(\theta), \tag{4.3}$$

https://doi.org/10.1017/jfm.2026.12015

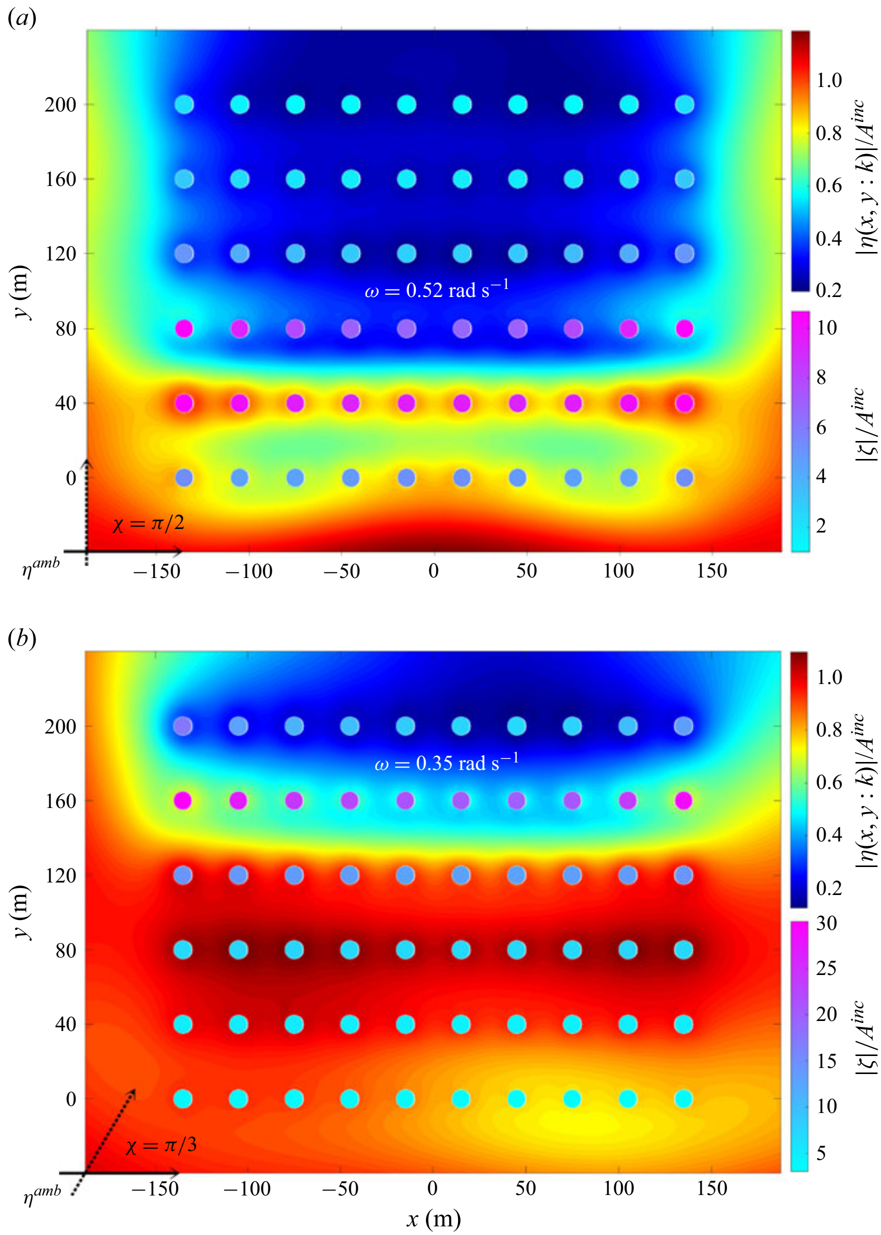

Figure 12. Surface elevations (upper colour bars) and WEC amplitudes (lower colour bars) in a finite array of $(J = 10) \times (K = 6) = 60$ WECs (table 2) for (*a*) $\omega = 0.52$ rad s^{-1} and $\chi = \pi/2$ rad, and (*b*) $\omega = 0.35$ rad s^{-1} and $\chi = \pi/3$ rad. The spatial location of frequency labels corresponds to (*a*) $\omega > \omega_0^3$ and (*b*) $\omega > \omega_0^5$.

which is such that the amplitude of a spectral component of width $\Delta\omega$ in frequency around ω, and $\Delta\theta$ in direction around θ, is (Chakrabarti 2005)

$$A(\omega, \theta) = \sqrt{2S(\omega, \theta)\, \Delta\omega\, \Delta\theta}. \tag{4.4}$$

https://doi.org/10.1017/jfm.2026.12015

The spectral density function $S_f(\omega)$ is chosen to be the JONSWAP (JOint North Sea WAve Project; Hasselmann *et al.* 1973) spectrum (Chakrabarti 2005)

$$S_f(\omega) = \frac{0.0081 g^2}{\omega^5} \mathrm{e}^{-1.25(\omega_p/\omega)^4} \gamma^r, \quad \text{where} \quad r = \mathrm{e}^{-(\omega-\omega_p)^2/(2\sigma^2\omega_p^2)}, \tag{4.5}$$

with peak frequency $\omega_p = 2\pi/T_p$ (i.e. maximum energy in the spectrum is at $\omega = 2\pi/T_p$) and spectral width

$$\sigma = \begin{cases} 0.007, & \omega < \omega_p, \\ 0.009, & \omega \geq \omega_p. \end{cases} \tag{4.6}$$

The sharpness of the spectrum is characterised by the peak enhancement factor γ. Globally, $\gamma = 1.54$ is typical of broadband sea states, particularly in coastal regions, while $\gamma = 3.3$ (narrower spectra) is typically used in the wave energy literature (Mazzaretto *et al.* 2022). The directional spreading function is modelled as a cosine-2ς distribution (Chakrabarti 2005)

$$D(\theta) = \frac{\Gamma(\varsigma+1)}{\sqrt{\pi}\,\Gamma(\varsigma+1/2)} \cos^{2\varsigma}(\theta-\chi) \quad \text{for} \quad 0 \leq |\theta-\chi| < \pi/2, \tag{4.7}$$

which is characterised by a spreading parameter ς, where $\varsigma = 1$ defines broadly spread sea states in direction (e.g. figure 13*b*), and $\varsigma = 4$ defines more narrowly spread sea states (e.g. figure 13*a*). The mean incident direction is set to be normal to the array ($\chi = \pi/2$ rad).

The proportion of the incident spectrum absorbed by the array is defined as α_{spec}, where

$$0 \leq \alpha_{spec} = \frac{\iint CW_{finite}(\omega, \theta)\, |A(\omega, \theta)|^2 \,\mathrm{d}\omega\, \mathrm{d}\theta}{\iint |A(\omega, \theta)|^2 \,\mathrm{d}\omega\, \mathrm{d}\theta} \lesssim 1. \tag{4.8}$$

The double integrals on the right-hand side of (4.8) are approximated using the trapezoidal rule. Figure 13(*c*) shows the proportion of the incident spectrum absorbed by the graded array of 60 WECs versus $T_p \in [5, 22]$ s, and for narrow ($\gamma = 3.3$ and $\varsigma = 4$) and broad ($\gamma = 1.54$ and $\varsigma = 1$) spectra. The target frequency interval corresponds to the wave period interval (9.6, 20.9] s (green shaded region in figure 13*c*). For $T_p = 10$ s (the narrow spectrum shown in figure 13*a*), 72 % of the incident spectrum is captured, as a large proportion of the spectrum lies below the target wave period interval (above the target frequency interval). In comparison, for $T_p = 17$ s (the broad spectrum shown in figure 13*b*), 95 % of the incident spectrum is captured, as the majority of the spectrum lies within the target interval.

The absorptions of three different uniform arrays are also shown in figure 13(*c*), and represent arrays designed for a particular wave climate. The arrays are tuned to resonate (fixed PTO parameters) at $T_0 = 10$, 15, 20 s, respectively. As expected, the absorptions of the uniform arrays peak for spectra with peak periods similar to the resonant frequencies, although when T_p is slightly greater than T_0. The peaks are $\alpha_{spec} = 0.48$–0.71, but drop as low as 0.07–0.20 over the target interval. In general, the peak absorption is considerably lower than the graded array, where the broadband design ensures efficient capture over a much larger proportion of frequencies within a spectrum.

Figure 14 shows the absorption of a uniform array that is retuned (replicating dynamic PTO parameters) to be resonant at every peak period (i.e. absorption of a spectrum when $T_0 = T_p$) on the target interval that lies within the designed frequency range of the graded array (i.e. up to $T_p = 10.3$ s, which coincides with the highest resonant frequency in the graded array). Again, the graded array (fixed PTO parameters) significantly outperforms the uniform array over the target interval. Similar absorption is obtained near $T_p \approx 10.3$ s,

https://doi.org/10.1017/jfm.2026.12015

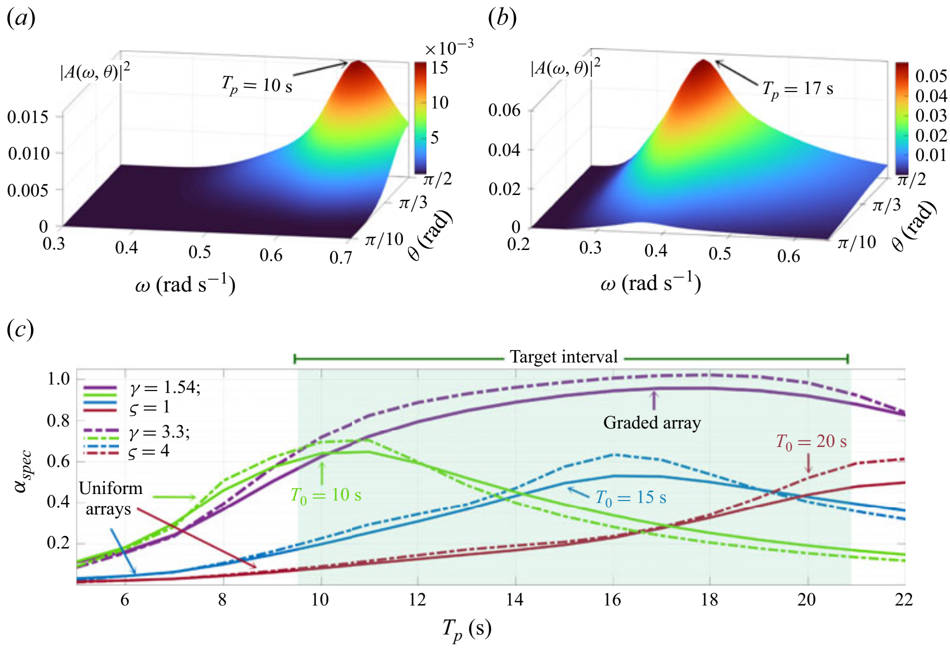

Figure 13. (a,b) Example incident spectra with significant wave height $H_s = 1$ m (average height of the highest third of waves; Chakrabarti 2005), for (a) $\gamma = 3.3$, $\varsigma = 4$ (dash-dotted) and $T_p = 10$ s, and (b) $\gamma = 1.54$, $\varsigma = 1$ (solid) and $T_p = 17$ s, over target frequency and direction intervals. (c) Proportion of the spectra absorbed by the graded array (purple) of $(J = 10) \times (K = 6) = 60$ WECs (table 2) with $W_x = 30$ m and $W_y = 40$ m, and for uniform arrays tuned to $T_0 = 10$ s (green), $T_0 = 15$ s (blue) and $T_0 = 20$ s (red).

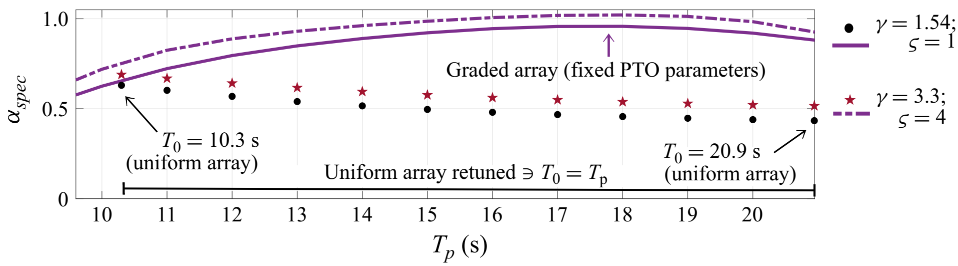

Figure 14. The α_{spec} of narrow ($\gamma = 3.3$, $\varsigma = 4$, purple dash-dotted) and broad ($\gamma = 1.54$, $\varsigma = 1$, purple solid) spectra by the graded array (fixed PTO parameters; table 2) is shown for $T_p \in [9.6, 20.9]$ s. The α_{spec} of the narrow (stars) and broad (dots) spectra by a uniform array is shown for comparison at each T_p. The uniform array is retuned (resonance T_0) to every T_p within the designed range of the graded array (i.e. $T_0 = T_p \in [10.3, 20.9]$ s).

where a large proportion of the spectrum lies above the designed frequency range of the graded array. On average, the graded array captures 33.45 % more of the broad spectra, and 33.01 % more of the narrow spectra, over the target interval than a dynamically retuned uniform array.

5. Discussion and conclusions

The ability to create broadband absorption of ocean wave energy from WEC arrays using the concepts of rainbow reflection and absorption has been extended to a 3-D model. The

https://doi.org/10.1017/jfm.2026.12015

approach was applied to arrays of heaving-buoy-type WECs by grading their resonant properties through attached PTO mechanisms. The WECs were arranged into rows, each of which contained infinitely many identical and equally spaced WECs, with a small periodicity length relative to the target wavelengths, to transform the wave field into a discrete directional spectrum. The chosen properties of the rows, relative to the incident waves, were such that a single propagating mode is supported, but the methods used could also be applied in the case that multiple modes are supported. An effective bandgap was generated over the target interval for low transmission, by grading the PTO spring constants of WECs in successive rows from high to low in the direction of the incident wave (normal incidence), to create a rainbow reflecting array. The PTO damping was tuned to capture the reflected wave energy for rainbow absorption by manipulating the location of the complex zeros in reflection for each row in the complex frequency plane. Over 10–20 s wave periods, average absorptions exceeding 94 % were achieved by arrays of 5–6 rows at normal incidence (or 98 % with ten rows), with the average absorption remaining >90 % for a wide range of incident wave directions. Similarly to the 2-D study by Westcott *et al.* (2024), the selection of PTO parameters could be automated by applying an optimisation algorithm, or optimised for even greater absorption, although the expected minimal gains to be made come at high computational expense in three dimensions, and require an informed initial solution.

In the 3-D model, the spacing within and between rows must be chosen, which has implications for controlling transmission, and the number of rows required to achieve a desired absorption. To control reflection and transmission over the target interval for high efficiency using a relatively small number of rows, the separation distances between WECs, within and between rows, were restricted to lie between three and eight times the WEC radius, as a closer spacing is unlikely to be feasible in practice, while a wider spacing decreases efficiency. The within-row spacing is connected to the resonance bandwidth of rows, and influences the ability to control the location of pole–zero pairs in complex frequency space. Rows with closely spaced WECs are stronger reflectors, and sustain low transmission over a wider frequency range as a result of broader resonance bandwidths. The resonant properties of the individual WECs influence the choice of spacing. Increasing the number of rows can compensate for higher transmission at wider spacings within rows (W_x) or narrower resonance bandwidths. However, similar to the 2-D case, the precise control of reflection and transmission zeros is limited by strong interactions between an increasing number of rows on a fixed frequency interval (Westcott *et al.* 2024). The maximum spacing between rows (W_y) is restricted by the second passband, which must occupy some minimum width in frequency space, and should be sufficiently small to prevent Bragg resonance from encroaching on the target interval. The ability to decrease this width via the grading depends on W_x and requires strongly reflective rows (small W_x) to prevent resonances associated with the second passband raising transmission near the upper bound of the target interval and causing absorption to drop. If both W_x and W_y are increased, these resonances can become interspersed between the row resonances, and potentially allow transmission to rise on the targeted interval.

To develop practical array designs, the infinite number of WECs in each row were truncated to a finite number of WECs. Finite arrays with 60 WECs (ten WECs per row) were shown to execute the strategies for broadband absorption. The rainbow absorbing design enables the finite array to achieve efficient, broadband absorption over broad directional bands, without retuning the WECs, which produces high efficiency in realistic sea states. The graded array outperforms uniform arrays tuned to the peak period of incident spectra covering the designed frequency range of the graded array, as the

https://doi.org/10.1017/jfm.2026.12015

broadband design ensures the capture of a much higher proportion of both narrow and broadly spread spectra.

The low transmission generated by the graded array could provide coastal protection benefits in addition to power capture. Graded arrays have garnered recent attention for their ability to generate broadband attenuation for coastal protection, and include graded arrays of non-absorbing submerged bars (Xu *et al.* 2023; Xie *et al.* 2025), bottom-mounted cylinders (Zhou & Song 2025), resonant C-shaped cylinders (Bennetts *et al.* 2018; Cao *et al.* 2025) and floating plates with attached resonators (Liu *et al.* 2025). Consequently, WEC arrays capable of providing the required attenuation, while also generating power, are an attractive prospect. Since the grading is implemented via the PTO mechanisms in the WEC array, rather than a surrounding structure, the array can be retuned if desired. This offers the additional flexibility to alternate between protecting coastlines or generating power, as proposed by Battisti *et al.* (2024) and Cui *et al.* (2024).

For linear theory to remain valid, the strategies presented are restricted to incident waves with small amplitudes. For the heaving buoys considered in this study, the incident amplitudes should be small enough that the resonating WECs do not break the water surface (i.e. the WEC amplitudes do not exceed the WEC draught). Future research directions include approximating nonlinearities such as drag, which will reduce WEC motions and therefore efficiency, and introducing physical constraints on WEC motions to remain within practical limitations as the incident amplitude increases. Based on recent demonstrations of non-absorbing graded arrays (e.g. Archer *et al.* 2020; Cao *et al.* 2025; Zhou & Song 2025), it is likely that the broadband control will remain effective when subject to nonlinear effects, but absorption will decline.

In conclusion, leveraging insights into the resonant interaction of water waves with periodic arrays of floating bodies (undergoing heaving motion), we have shown that arrays of heaving buoys can be designed for efficient broadband absorption, without the use of optimisation algorithms, by grading their resonant properties for rainbow absorption. Array designs were presented that capture over 90 % of the incident energy from two-thirds of usable ocean wave frequencies, and for incident wave directions ranging up to $\pi/3$ rad from normal incidence, using fixed PTO parameters. The key properties of the rainbow absorbing design extend effectively to finite arrays with a reasonably small number of WECs per row. The practical design for finite arrays demonstrates highly efficient power capture in realistic sea states that are broadly spread in both frequency and direction.

Acknowledgements. The authors thank R. Alwan for code towards the single-body problem. An early version of this work, namely Westcott *et al.* (2025), was presented at the 40th International Workshop on Water Waves and Floating Bodies in Shanghai, China.

Funding. This work was funded by the Australian Research Council (ARC) (grant no. LP180101109). A.-R.W. was supported by the Commonwealth through an Australian Government Research Training Program Scholarship [DOI: https://doi.org/10.82133/C42F-K220] and a University of Adelaide Research Scholarship. L.G.B. is the recipient of an ARC Mid-career Fellowship (FT190100404). N.Y.S. is the recipient of an ARC Early Career Industry Fellowship (IE230100545).

Declaration of interests. The authors report no conflict of interest.

Appendix A. Single-cell problem: truncated cylinder

The diffraction and radiation problems are individually solved using separation of variables, subject to the respective boundary conditions (3.8) on the wetted surface of the WEC, and are combined to return the full wave field

$$\varphi(r, \theta, z) = \varphi^{inc}(r, \theta, z) + \varphi^{diff}(r, \theta, z) + \zeta\, \varphi^{rad}(r, \theta, z). \tag{A1}$$

https://doi.org/10.1017/jfm.2026.12015

The fluid domain is divided into interior ($r \le L$) and exterior ($r \ge L$) regions about the interface $r = L$, at the sides of the WEC (cylinder's radius). In the exterior region (superscript E),

$$\varphi^E = \sum_{n=0}^{\infty} Z_n(z) \sum_{\mu=-\infty}^{\infty} \left[A_{n\mu}\, I_\mu(\kappa_n r) + \hat{D}^{diff}_{n\mu} \frac{K_\mu(\kappa_n r)}{K_\mu(\kappa_n L)} \right] \mathrm{e}^{\mathrm{i}\mu\theta} + \zeta \sum_{n=0}^{\infty} Z_n(z)\, \hat{D}^{rad}_{n0} \frac{K_0(\kappa_n r)}{K_0(\kappa_n L)}, \tag{A2}$$

where I_μ and K_μ are modified Bessel functions of the first and second kind, respectively, and are of order μ, and κ_n are defined in terms of the wavenumbers k_n such that $\kappa_n = -\mathrm{i}k_n$, $n \in \mathbb{Z}$, $n \ge 0$, for ease of notation. The known amplitudes associated with the ambient incident wave are denoted $A_{n\mu}$. The unknown diffraction $\hat{D}^{diff}_{n\mu}$ and radiation $\hat{D}^{rad}_{n0}$ coefficients are normalised against the cylinder's sides. There is no angular dependence ($\mu = 0$) in the radiation problem, as heave radiation is symmetric. In the interior region (superscript I),

$$\varphi^I = \sum_{n=0}^{\infty} \mathcal{Z}_n(z) \sum_{\mu=-\infty}^{\infty} d^{diff}_{n\mu} \frac{I_\mu(\varkappa_n r)}{I_\mu(\varkappa_n L)} \mathrm{e}^{\mathrm{i}\mu\theta} + \zeta \left[\sum_{n=0}^{\infty} \mathcal{Z}_n(z)\, d^{rad}_{n0} \frac{I_0(\varkappa_n r)}{I_0(\varkappa_n L)} + \frac{\omega^2 \left[(z+h)^2 - r^2/2 \right]}{2g(h-L)} \right], \tag{A3}$$

where $d^{diff}_{n\mu}$ and d^{rad}_{n0} are the unknown coefficients in the diffraction and radiation problems, respectively. The last term is the particular solution in the radiation problem, which satisfies the boundary conditions (3.8) on the WEC. The vertical eigenfunctions are given by

$$\mathcal{Z}_n(z) = \frac{\cosh(\mathrm{i}\varkappa_n(z+h))}{\cosh(\mathrm{i}\varkappa_n(h-L))} \quad \text{for} \quad \varkappa_n = \frac{n\pi}{h-L}. \tag{A4}$$

Truncating the infinite summations at $n = N-1$ and $\mu = \pm U$ modes (chosen to be sufficient for convergence), a diffraction transfer matrix $\boldsymbol{B}$ is defined such that $(\boldsymbol{D}^{diff} + \zeta\, \boldsymbol{D}^{rad}) = \boldsymbol{BA}$ for a given incident wave with amplitude $\boldsymbol{A}$, where the elements of $[\boldsymbol{D}^{diff} + \zeta\, \boldsymbol{D}^{rad}]_{n\mu} = (\hat{D}^{diff}_{n\mu} + \zeta\, \hat{D}^{rad}_{n\mu})/K_\mu(\kappa_n L)$ are generated from the as yet unknown diffraction and radiation coefficients of the scattered potential,

$$\varphi^{scat} = \sum_{n=0}^{N-1} Z_n(z) \sum_{\mu=-U}^{U} \left[\hat{D}^{diff}_{n\mu} + \zeta\, \hat{D}^{rad}_{n\mu} \right] \frac{K_\mu(\kappa_n r)}{K_\mu(\kappa_n L)} \mathrm{e}^{\mathrm{i}\mu\theta}, \quad \text{where} \quad \hat{D}^{rad}_{n\mu} = 0 \text{ for all } \mu \ne 0. \tag{A5}$$

The eigenfunction expansion matching method is used to determine the unknown coefficients by enforcing continuity of pressure and horizontal velocity at the interface $r = L$ between the interior φ^I and exterior φ^E regions (Linton & McIver 2001):

$$\varphi^E = \varphi^I \quad \text{on} \quad z \in (-h, -L), \tag{A6}$$

$$\frac{\partial \varphi^E}{\partial r} = \begin{cases} \dfrac{\partial \varphi^I}{\partial r} & \text{on } z \in (-h, -L), \\ 0 & \text{on } z \in (-L, 0). \end{cases} \tag{A7}$$

Systems of equations for the unknown coefficients are obtained by multiplying (A6) and (A7) by the test function $\mathcal{Z}_m$, and integrating over $z \in (-h, -L)$ and $z \in (-h, 0)$, respectively.

https://doi.org/10.1017/jfm.2026.12015

A.1. *The diffraction problem*

In the diffraction problem, the resulting system of equations is given by

$$\sum_{n=0}^{N-1}\sum_{\mu=-U}^{U}\left[\mathcal{A}_{mn}d_{n\mu}^{diff}\,\mathrm{e}^{\mathrm{i}\mu\theta}-\mathcal{B}_{mn}\hat{D}_{n\mu}^{diff}\,\mathrm{e}^{\mathrm{i}\mu\theta}\right]=\sum_{n=0}^{N-1}\sum_{\mu=-U}^{U}\mathcal{B}_{mn}A_{n\mu}I_{\mu}(\kappa_n L)\,\mathrm{e}^{\mathrm{i}\mu\theta},$$
$$\sum_{n=0}^{N-1}\sum_{\mu=-U}^{U}\left[\mathcal{B}_{mn}\varkappa_n d_{n\mu}^{diff}\frac{I'_{\mu}(\varkappa_n L)}{I_{\mu}(\varkappa_n L)}-\mathcal{F}_{mn}k_n\hat{D}_{n\mu}^{diff}\frac{K'_{\mu}(\kappa_n L)}{K_{\mu}(\kappa_n L)}\right]=\sum_{n=0}^{N-1}\sum_{\mu=-U}^{U}\mathcal{F}_{mn}k_n A_{n\mu}\,I'_{\mu}(\kappa_n L), \tag{A8}$$

where the (m, n) elements of the $M \times N$ matrices $\mathcal{A}$, $\mathcal{B}$, $\mathcal{F}$ are, respectively,

$$\mathcal{A}_{mn}=\int_{-h}^{-d}\mathcal{Z}_m\mathcal{Z}_n\,\mathrm{d}z,\quad \mathcal{B}_{mn}=\int_{-h}^{-d}\mathcal{Z}_m Z_n\,\mathrm{d}z,\quad \mathcal{F}_{mn}=\int_{-h}^{0}Z_m Z_n\,\mathrm{d}z. \tag{A9}$$

For future reference, we note that the diffraction transfer matrices relating the incident and scattered waves in the interior ($\boldsymbol{B}^{int}$) and exterior ($\boldsymbol{B}^{diff}$) regions are retrieved from $[\boldsymbol{d}^{diff}\ \boldsymbol{D}^{diff}]^{\mathrm{T}}=[\boldsymbol{B}^{int}\ \boldsymbol{B}^{diff}]^{\mathrm{T}}[\boldsymbol{A}\ \boldsymbol{A}]^{\mathrm{T}}$. For each Fourier mode μ, the (m, n) term for $m, n = 1, 2, \ldots, N$ is defined by

$$\boldsymbol{B}_{\mu}^{diff}=(B_{mn})=\left(\frac{K'_{\mu}(\kappa_n L)}{K_{\mu}(\kappa_n L)}\mathcal{F}_{mn}\right)^{-1}\left(\frac{\varkappa_n}{k_n}\frac{I'_{\mu}(\varkappa_n L)}{I_{\mu}(\varkappa_n L)}\mathcal{B}_{mn}[M_1^{-1}M_2]-I'_{\mu}(\kappa_n L)\mathcal{F}_{mn}\right) \tag{A10}$$

and $\boldsymbol{B}_{\mu}^{int}=(B_{mn})=[M_1^{-1}M_2]$, where

$$M_1=\mathcal{A}_{mn}-\mathcal{B}_{mn}\left(\frac{K'_{\mu}(\kappa_n L)}{K_{\mu}(\kappa_n L)}\mathcal{F}_{mn}\right)^{-1}\mathcal{B}_{mn}\frac{\varkappa_n}{k_n}\frac{I'_{\mu}(\varkappa_n L)}{I_{\mu}(\varkappa_n L)}, \tag{A11}$$

$$M_2=\mathcal{B}_{mn}I_{\mu}(\kappa_n L)-\mathcal{B}_{mn}\left(\frac{K'_{\mu}(\kappa_n L)}{K_{\mu}(\kappa_n L)}\mathcal{F}_{mn}\right)^{-1}\mathcal{F}_{mn}I'_{\mu}(\kappa_n L). \tag{A12}$$

A.2. *The radiation problem*

The system of equations for the radiation problem is given by

$$\sum_{n=0}^{N-1}\mathcal{A}_{mn}d_{n0}^{rad}-\sum_{n=0}^{N-1}\mathcal{B}_{mn}\hat{D}_{n0}^{rad}=F_1$$
$$\sum_{n=0}^{N-1}\mathcal{B}_{mn}\varkappa_n d_{n0}^{rad}\frac{I'_0(\varkappa_n L)}{I_0(\varkappa_n L)}-\sum_{n=0}^{N-1}\mathcal{F}_{mn}k_n\hat{D}_{n0}^{rad}\frac{K'_0(\kappa_n L)}{K_0(\kappa_n L)}=F_2, \tag{A13}$$

where F_1 and F_2 are associated with the particular solution, and are calculated as

$$F_1=-\sum_{m=0}^{N-1}\int_{-h}^{-L}\frac{\omega^2}{2g(h-L)}\left[(z+h)^2-\frac{L^2}{2}\right]\frac{\cosh(\mathrm{i}\varkappa_m(z+h))}{\cosh(\mathrm{i}\varkappa_m(h-L))}\,\mathrm{d}z, \tag{A14}$$

$$F_2=\sum_{m=0}^{N-1}\int_{-h}^{0}Z_m(z)\,\frac{\omega^2 L}{2g(h-L)}\,\mathrm{d}z, \tag{A15}$$

https://doi.org/10.1017/jfm.2026.12015

assuming unit heave amplitude $\zeta = 1$. The heave amplitude of the WEC is calculated from the equation of motion (3.9), given the hydrodynamic forcing on the body

$$\iint_{S_B} \varphi n \,\mathrm{d}S = \int_0^L \int_0^{2\pi} \varphi^{diff} r \,\mathrm{d}\theta \,\mathrm{d}r + \int_0^L \int_0^{2\pi} \zeta \varphi^{rad} r \,\mathrm{d}\theta \,\mathrm{d}r \quad \text{at } z = -L. \tag{A16}$$

The radiation forcing $F^{rad} = \int_0^L \int_0^{2\pi} \varphi^{rad} r \,\mathrm{d}\theta \,\mathrm{d}r$ is evaluated at $z = -L$:

$$\begin{aligned}\int_0^L \int_0^{2\pi} \varphi^{rad} r \,\mathrm{d}\theta \,\mathrm{d}r &= \int_0^L \int_0^{2\pi} \left[\sum_n \left(d_{n0}^{rad} \frac{I_0(\varkappa_n r)}{I_0(\varkappa_n L)} \right) r + \frac{\omega^2}{g} \left(\frac{r(h-L)^2}{2(h-L)} - \frac{r^3}{4(h-L)} \right) \right] \mathrm{d}\theta \,\mathrm{d}r \\ &= 2\pi \sum_n d_{n0}^{rad} \frac{L}{\varkappa_n} \frac{I_1(\varkappa_n L)}{I_0(\varkappa_n L)} + 2\pi \frac{\omega^2}{g} \left[\frac{L^2(h-L)^2}{4(h-L)} - \frac{L^4}{16(h-L)} \right].\end{aligned} \tag{A17}$$

The components of F^{rad} in phase with the acceleration and velocity of the body, respectively, correspond to the added mass $a(\omega)$ and radiation damping $b(\omega)$, and are given by

$$a(\omega) = \rho g \,\mathrm{Re}(F^{rad})/\omega^2 \quad \text{and} \quad b(\omega) = \rho g \,\mathrm{Im}(F^{rad})/\omega. \tag{A18}$$

The excitation forcing F^{exc} results from the hydrodynamic pressure on the underside of a WEC ($z = -L$) for a given incident wave in the diffraction problem, where $\boldsymbol{d}^{diff} = \boldsymbol{B}_{\mu=0}^{int} \boldsymbol{A}$:

$$\begin{aligned}F^{exc} = \rho g \int_0^L \int_0^{2\pi} \varphi^{diff} r \,\mathrm{d}\theta \,\mathrm{d}r &= 2\pi \rho g \sum_n d_{n0}^{diff} \frac{I_1(\varkappa_n L)}{I_0(\varkappa_n L)} \frac{L}{\varkappa_n} \\ &= \boldsymbol{V} \boldsymbol{d}^{diff} = \left[\boldsymbol{V} \boldsymbol{B}_0^{int} \right] \boldsymbol{A} \\ &= \boldsymbol{f_e} \boldsymbol{A}.\end{aligned} \tag{A19}$$

As an aside, note that F^{exc} is determined by replacing $\boldsymbol{A}$ with the vector of amplitudes $\boldsymbol{C}$ in an array, corresponding to the incident field which accounts for all interactions within the array. The heave amplitude is expressed as a $1 \times N$ vector

$$\boldsymbol{\zeta} = \left[-\omega^2(\mathfrak{M} + a(\omega)) - \mathrm{i}\omega\,(b(\omega) + B_{PTO}) + (\mathfrak{C} + C_{PTO}) \right]^{-1} \boldsymbol{f_e}, \tag{A20}$$

where the PTO spring constant C_{PTO} is chosen to tune the WEC resonance to a prescribed frequency ω_0, i.e.

$$C_{PTO} = \omega_0^2\,(\mathfrak{M} + a(\omega_0)) - \mathfrak{C}. \tag{A21}$$

An $N \times N$ matrix $\boldsymbol{B}^{rad}$, defined for the $\mu = 0$ Fourier mode, is obtained using the $N \times 1$ vector of radiation coefficients in the exterior region

$$\boldsymbol{d}^{rad} \zeta = \boldsymbol{d}^{rad} \boldsymbol{\zeta} \boldsymbol{A} = \boldsymbol{B}^{rad} \boldsymbol{A}. \tag{A22}$$

A.3. *The diffraction transfer matrix*

The diffraction transfer matrix $\boldsymbol{B} = \boldsymbol{B}^{diff} + \boldsymbol{B}^{rad}$, where $(B_{\mu mn}^{rad}) = 0 \;\forall\, \mu \neq 0$, encapsulates the scattering properties of the WEC, forming an $N \times (2U + 1)$ square matrix

https://doi.org/10.1017/jfm.2026.12015

$$\boldsymbol{B} = \begin{bmatrix} \boldsymbol{B}^{\mu}_{00} & \boldsymbol{B}^{\mu}_{01} & \cdots & \boldsymbol{B}^{\mu}_{0(N-1)} \\ \boldsymbol{B}^{\mu}_{10} & \boldsymbol{B}^{\mu}_{11} & \cdots & \boldsymbol{B}^{\mu}_{1(N-1)} \\ \vdots & \vdots & \ddots & \vdots \\ \boldsymbol{B}^{\mu}_{(N-1)0} & \boldsymbol{B}^{\mu}_{(N-1)1} & \cdots & \boldsymbol{B}^{\mu}_{(N-1)(N-1)} \end{bmatrix}. \tag{A23}$$

The elements of the diagonal matrix $\boldsymbol{B}^{\mu}_{mn}$ are given in (A10) when $\mu \neq 0$, with the elements in (A22) added when $\mu = 0$, such that for $m, n = 0, 1, \ldots, N-1$,

$$\boldsymbol{B}^{\mu}_{mn} = \begin{bmatrix} \boldsymbol{B}^{-U}_{mn} & 0 & \cdots & 0 \\ 0 & \boldsymbol{B}^{-U+1}_{mn} & \cdots & 0 \\ \vdots & \vdots & \ddots & \vdots \\ 0 & 0 & \cdots & \boldsymbol{B}^{U}_{mn} \end{bmatrix}. \tag{A24}$$

Appendix B. The PWE

The velocity potential around a row of WECs is obtained by summing the scattered wave fields of all WECs in the row in terms of their local coordinate systems

$$\phi(x, y, z) = \varphi^{inc}(r, \theta, z) + \sum_{n=0}^{\infty} Z_n(z) \sum_{j=-\infty}^{\infty} \mathcal{Q}_j \sum_{\mu=-\infty}^{\infty} D_{n\mu}\, K_{\mu}(\kappa_n r_j)\, \mathrm{e}^{\mathrm{i}\mu\theta_j}. \tag{B1}$$

Following Peter *et al.* (2006), the modified Bessel functions are replaced with an integral representation to express the scattered field as a PWE

$$\varphi^{scat}(r, \theta, z) = \sum_{n=0}^{\infty} Z_n(z) \sum_{m=-\infty}^{\infty} \mathcal{D}^{\pm}_{mn}\, \mathrm{e}^{\mathrm{i}k_n r \cos(\theta \mp \chi_{mn})} \quad \text{for} \quad \pm y > L, \tag{B2}$$

where

$$\mathcal{D}^{\pm}_{mn} = \frac{\mathrm{i}\pi}{k_n W_x} \frac{1}{\sin(\chi_{mn})} \sum_{\mu=-\infty}^{\infty} D_{n\mu}\, \mathrm{e}^{\pm \mathrm{i}\mu\chi_{mn}} \tag{B3}$$

are the scattered amplitudes of wave modes that propagate or decay in the $\pm y$-direction. For all k_0 and W_x considered, $\sin(\chi_{mn}) \neq 0$ (i.e. the propagation of a scattered mode $\chi_{mn} = 0$ or π rad along the row when a scattering angle cuts-on (Linton & Thompson 2007) does not occur here due to the W_x-to-wavelength ratios). Truncating the infinite summations at $n = N_0$ and $|\mu| = U$, the scattered amplitudes are obtained from

$$\boldsymbol{D} = \left[\boldsymbol{I} - \boldsymbol{B}\boldsymbol{\sigma}\right]^{-1} \boldsymbol{B}\boldsymbol{A}, \tag{B4}$$

where $\boldsymbol{\sigma}$ is an $N \times (2U+1)$ diagonal matrix $\boldsymbol{\sigma} = \mathrm{diag}[\hat{\boldsymbol{\sigma}}^0\ \hat{\boldsymbol{\sigma}}^1\ \ldots\ \hat{\boldsymbol{\sigma}}^{(N_0-1)}]$. The sub-matrices $\hat{\boldsymbol{\sigma}}^n$ have elements $\sigma^n_{\mu-\tau}$ defined in (3.22), such that

https://doi.org/10.1017/jfm.2026.12015

$$\begin{array}{c} \qquad\qquad \mu = -U, \dots, U \longrightarrow \\ \hat{\boldsymbol{\sigma}}^n = \begin{bmatrix} \sigma^n_{-U-(-U)} & \sigma^n_{-U+1-(-U)} & \cdots & \sigma^n_{U-(-U)} \\ \sigma^n_{-U-(-U+1)} & \sigma^n_{-U+1-(-U+1)} & \cdots & \sigma^n_{U-(-U+1)} \\ \vdots & & \ddots & \vdots \\ \sigma^n_{-U-(U)} & \sigma^n_{-U+1-(U)} & \cdots & \sigma^n_{U-(U)} \end{bmatrix} \Big\downarrow \tau = -U, \dots, U. \end{array} \tag{B5}$$

The infinite summations in the PWE (B2) are truncated to $N_1 \leq N_0$ vertical modes and $M = p + q + 1$ scattering angles (which includes complex scattering angles). Here, N_1 and M are selected such that the PWE has converged to the full solution at the midpoint between rows for all frequencies considered. The $(M \times N_1)$ square reflection and transmission matrices, $\boldsymbol{R}$ and $\boldsymbol{T}$, respectively, are generated by treating the ith scattering angle ($i \in [-p, q]$) and the jth vertical mode ($j \in [0, N_1]$) as incident, and calculating the (mn)th scattered mode ($m = -p, \dots, q$, $n = 0, \dots, N_1$) as

$$R^{ij}_{mn} = \frac{\mathrm{i}\pi}{k_n W_x} \frac{1}{\sin(\chi_{mn})} \sum_{\mu=-U}^{U} D^{ij}_{n\mu}\, \mathrm{e}^{-\mathrm{i}\mu\chi_{mn}}, \tag{B6}$$

$$T^{ij}_{mn} = \delta_{jn} + \frac{\mathrm{i}\pi}{k_n W_x} \frac{1}{\sin(\chi_{mn})} \sum_{\mu=-U}^{U} D^{ij}_{n\mu}\, \mathrm{e}^{\mathrm{i}\mu\chi_{mn}}, \tag{B7}$$

where $\delta_{jn} = 1$ for $n = j$, and zero otherwise. The $D^{ij}_{n\mu}$ are obtained by setting $[\boldsymbol{A}]_{n\mu} = A^{ij}_{n\mu}$ to

$$A^{ij}_{n\mu} = \begin{cases} (-1)^{\mu}\, \mathrm{e}^{-\mathrm{i}\mu\chi_i} & n = j, \\ 0 & n \neq j, \end{cases} \tag{B8}$$

for $n, j = 0, 1, \dots, N_1$. The entries of the reflection matrix (analogous for $\boldsymbol{T}$) are

$$\boldsymbol{R} = \begin{bmatrix} R^{-p0}_{-p0} & R^{-p1}_{-p0} & \cdots & R^{-pN_1}_{-p0} & \cdots & R^{qN_1}_{-p0} \\ R^{-p0}_{-pN_1} & R^{-p1}_{-pN_1} & \cdots & R^{-pN_1}_{-pN_1} & \cdots & R^{qN_1}_{-pN_1} \\ \vdots & \vdots & \ddots & \vdots & \ddots & \vdots \\ R^{-p0}_{qN_1} & R^{-p1}_{qN_1} & \cdots & R^{-pN_1}_{qN_1} & \cdots & R^{qN_1}_{qN_1} \end{bmatrix}. \tag{B9}$$

Appendix C. Solution method for finite arrays

In finite arrays, the scattered coefficients of each WEC are obtained by replacing the lattice sums in (3.22) with $(N_0 + 1) \times (2U + 1)$ square separation matrices $\boldsymbol{\sigma}_{jl} = (-1)^{\mu}\, K_{\tau-\mu}(\kappa_n W_{jl})\, \mathrm{e}^{\mathrm{i}(\tau-\mu)\vartheta_{j-l}}$, where $(W_{jl}, \vartheta_{j-l})$ specifies the location of WEC l in the local coordinate system of WEC j (Martin 2006). For an array with $J \times K$ WECs, the scattered coefficients are calculated from

$$\left[\boldsymbol{D}^1\ \boldsymbol{D}^2\ \cdots\ \boldsymbol{D}^{JK}\right]^{\mathrm{T}} = [\boldsymbol{I} - \mathcal{B}]^{-1} \left[\boldsymbol{B}^1 \boldsymbol{A}^1\ \ \boldsymbol{B}^2 \boldsymbol{A}^2\ \cdots\ \boldsymbol{B}^{JK} \boldsymbol{A}^{JK}\right]^{\mathrm{T}}, \tag{C1}$$

https://doi.org/10.1017/jfm.2026.12015

where the (j, l) sub-matrix of the matrix $\mathcal{B}$ is defined as $[\mathcal{B}]_{jl} = \boldsymbol{B}^j \boldsymbol{\sigma}_{jl}$. The vector of incident amplitudes for WEC j, where $j = 1, 2, \ldots, JK$, has elements defined by $[\boldsymbol{A}^j]_{n\mu} = \exp(\mathrm{i}k_0 W_{j0} \cos(\vartheta_j - \chi))\, A_{n\mu}$, where (W_{j0}, ϑ_{j0}) specifies the position of WEC j in global coordinates (Kagemoto & Yue 1986).

References

Archer, A.J., Wolgamot, H.A., Orszaghova, J., Bennetts, L.G., Peter, M.A. & Craster, R.V. 2020 Experimental realization of broadband control of water-wave-energy amplification in chirped arrays. *Phys. Rev. Fluids* **5** (6), 062801.

Battisti, B., Giorgi, G. & Fernandez, G.V. 2024 Balancing power production and coastal protection: a bi-objective analysis of wave energy converters. *Renew. Energy* **220**, 119702.

Bennetts, L.G., Peter, M.A. & Craster, R.V. 2018 Graded resonator arrays for spatial frequency separation and amplification of water waves. *J. Fluid Mech.* **854**, R4.

Bennetts, L.G., Peter, M.A. & Craster, R.V. 2019 Low-frequency wave-energy amplification in graded two-dimensional resonator arrays. *Phil. Trans. R. Soc. Lond. A* **377** (2156), 20190104.

Bennetts, L.G., Peter, M.A., Squire, V.A. & Meylan, M.H. 2010 A three-dimensional model of wave attenuation in the marginal ice zone. *J. Geophys. Res. Oceans* **115**, C12043.

Bennetts, L.G. & Squire, V.A. 2009 Wave scattering by multiple rows of circular ice floes. *J. Fluid Mech.* **639**, 213–238.

Blanco, M., Villalba, I., Lafoz, M., Nájera, J., Navarro, G. & Santos-Herrán, M. 2025 Power optimization modelling as a computational tool for power take off design in wave energy converters. *Appl. Ocean Res.* **160**, 104628.

Cao, H., Chen, L.F., Ning, D.Z., Peng, C., Xu, J. & Lin, H.X. 2025 Broadband energy attenuation of long-period water waves by a graded array of C-shaped cylinders. In *The 40th International Workshop on Water Waves and Floating Bodies* (ed. X. Zhang), pp. 21–24.

Chakrabarti, S.K. 2005 Ocean environment. In *Handbook of Offshore Engineering* (ed. S.K. Chakrabarti), pp. 79–131. Elsevier.

Chou, T. 1998 Band structure of surface flexural–gravity waves along periodic interfaces. *J. Fluid Mech.* **369**, 333–350.

Coe, R.G., Bacelli, G. & Forbush, D. 2021 A practical approach to wave energy modeling and control. *Renew. Sustainable Energy Rev.* **142**, 110791.

CorPower Ocean. 2026 Wave energy technology - How CorPower Ocean's WEC Works. Available at: https://corpowerocean.com/technology/ (Accessed: 27-08-26).

Cui, L. *et al.* 2024 Protecting coastlines by offshore wave farms: on optimising array configurations using a corrected far-field approximation. *Renew. Energy* **224**, 120109.

Davies, B. *et al.* 2025 Roadmap on metamaterial theory, modelling and design. *J. Phys. D: Appl. Phys.* **58** (20), 203002.

Edwards, E.C. & Yue, D.K.-P. 2022 Optimisation of the geometry of axisymmetric point-absorber wave energy converters. *J. Fluid Mech.* **933**, A1.

Falnes, J. 2005 *Ocean Waves and Oscillating Systems: Linear Interactions Including Wave-Energy Extraction*. Cambridge University Press.

Falnes, J. & Budal, K. 1982 Wave-power absorption by parallel rows of interacting oscillating bodies. *Appl. Ocean Res.* **4** (4), 194–207.

Gallutia, D., Fard, M.T., Soto, M.G. & He, J. 2022 Recent advances in wave energy conversion systems: from wave theory to devices and control strategies. *Ocean Engng* **252**, 111105.

Gong, H., Zheng, S., Cao, F., Han, Z. & Shi, H. 2024 GWECS: an indicator to describe the energy absorption characteristics of wave energy converter arrays in real sea states. *Renew. Energy* **237**, 121483.

Göteman, M., Giassi, M., Engström, J. & Isberg, J. 2020 Advances and challenges in wave energy park optimization – a review. *Frontiers Energy Res.* **8**, 26.

Guo, B. & Ringwood, J.V. 2021 A review of wave energy technology from a research and commercial perspective. *IET Renew. Power Generation* **15** (14), 3065–3090.

Hasselmann, K. *et al.* 1973 Measurements of wind-wave growth and swell decay during the joint North Sea wave project (JONSWAP). *Ergänzung Dtsch. Hydrogr. Z. Reihe A* **8** (12), 1–95.

He, Z., Ning, D., Gou, Y. & Mayon, R. 2022 Optimization of a wave energy converter square array based on the differential evolution algorithm. *Ocean Engng* **262**, 112189.

Hu, Y., Cheng, Y., Dai, S., Yuan, Z. & Incecik, A. 2025 Broadband wave conversion by a 'Pan Flute'-type multi-oscillating-water-column (M-OWC) breakwater system. *Energy Convers. Manage.* **333**, 119820.

https://doi.org/10.1017/jfm.2026.12015

KAGEMOTO, H. & YUE, D.K.P. 1986 Interactions among multiple three-dimensional bodies in water waves: an exact algebraic method. *J. Fluid Mech.* **166**, 189–209.
KORDE, U.A. & RINGWOOD, J.V. 2016 *Hydrodynamic Control of Wave Energy Devices*. Cambridge University Press.
LINTON, C.M. 1998 The Green's function for the two-dimensional Helmholtz equation in periodic domains. *J. Engng Maths* **33** (4), 377–401.
LINTON, C.M. & MCIVER, P. 2001 *Handbook of Mathematical Techniques for Wave/Structure Interactions*. CRC Press.
LINTON, C.M. & THOMPSON, I. 2007 Resonant effects in scattering by periodic arrays. *Wave Motion* **44** (3), 165–175.
LIU, H., FARHAT, M., BAGCI, H., GUENNEAU, S. & WU, Y. 2025 Broadband water wave reflector with customisable frequency range enabled by floating metaplates. *J. Fluid Mech.* **1020**, A50.
MARTIN, P.A. 2006 *Multiple Scattering: Interaction of Time-Harmonic Waves with N Obstacles*, Encyclopedia of Mathematics and its Applications (ed. P. Flajolet, M.E.H. Ismail & E. Lutwak), vol. 107. Cambridge University Press.
MAZZARETTO, O.M., MENÉNDEZ, M. & LOBETO, H. 2022 A global evaluation of the JONSWAP spectra suitability on coastal areas. *Ocean Engng* **266**, 112756.
MCIVER, P. 1994 Some hydrodynamic aspects of arrays of wave-energy devices. *Appl. Ocean Res.* **16** (2), 61–69.
MCIVER, P. 2000 Water-wave propagation through an infinite array of cylindrical structures. *J. Fluid Mech.* **424**, 101–125.
MCPHEDRAN, R.C., BOTTEN, L.C., ASATRYAN, A.A., NICOROVICI, N.A., DE STERKE, C.M. & ROBINSON, P.A. 1999 Ordered and disordered photonic band gap materials. *Austral. J. Phys.* **52** (5), 791–809.
MEI, C.C., STIASSNIE, M. & YUE, D.K.-P. 2005 *Theory and Applications of Ocean Surface Waves: Part 1: Linear Aspects, Advanced Series on Ocean Engineering*, vol. 23. World Scientific Publishing.
MULHOLLAND, L.S. & HECKL, M.A. 1994 Multi-directional sound wave propagation through a tube bundle. *J. Sound Vib.* **176** (3), 377–398.
NING, D. & DING, B. (eds) 2022 *Modelling and Optimization of Wave Energy Converters*. CRC Press.
PECHER, A. & KOFOED, J.P. (eds) 2017 *Handbook of Ocean Wave Energy, Ocean Engineering & Oceanography*, vol. 7. Springer International Publishing.
PETER, M.A. & MEYLAN, M.H. 2010 Water-wave scattering by vast fields of bodies. *SIAM J. Appl. Maths* **70** (5), 1567–1586.
PETER, M.A., MEYLAN, M.H. & LINTON, C.M. 2006 Water-wave scattering by a periodic array of arbitrary bodies. *J. Fluid Mech.* **548**, 237–256.
RINGWOOD, J.V. 2025 Control co-design for wave energy systems. *Appl. Ocean Res.* **158**, 104514.
RINGWOOD, J.V., ZHAN, S. & FAEDO, N. 2023 Empowering wave energy with control technology: possibilities and pitfalls. *Annu. Rev. Control* **55**, 18–44.
ROMERO-GARCÍA, V., THEOCHARIS, G., RICHOUX, O. & PAGNEUX, V. 2016 Use of complex frequency plane to design broadband and sub-wavelength absorbers. *J. Acoust. Soc. Am.* **139** (6), 3395–3403.
SHARP, C. & DUPONT, B. 2018 Wave energy converter array optimization: a genetic algorithm approach and minimum separation distance study. *Ocean Engng* **163**, 148–156.
SHENG, W. & LEWIS, A. 2016 Power takeoff optimization for maximizing energy conversion of wave-activated bodies. *IEEE J. Ocean. Engng* **41** (3), 529–540.
TODALSHAUG, J.H., ÁSGEIRSSON, G.S., HJÁLMARSSON, E., MAILLET, J., MÖLLER, P., PIRES, P., GUÉRINEL, M. & LOPES, M. 2016 Tank testing of an inherently phase-controlled wave energy converter. *Intl J. Mar. Energy* **15**, 68–84.
WEGERT, E. 2012 *Visual Complex Functions: An Introduction with Phase Portraits*. Springer.
WESTCOTT, A.-R., BENNETTS, L.G., SERGIIENKO, N.Y. & CAZZOLATO, B.S. 2024 Broadband near-perfect capture of water wave energy by an array of heaving buoy wave energy converters. *J. Fluid Mech.* **998**, A5.
WESTCOTT, A.-R., BENNETTS, L.G., SERGIIENKO, N.Y., CAZZOLATO, B.S. & PETER, M.A. 2025 Broadband absorption of wave energy by graded arrays of heaving buoys in 3D. In *The 40th International Workshop on Water Waves and Floating Bodies* (ed. X. Zhang), pp. 185–188.
WILKS, B., MEYLAN, M.H., MONTIEL, F., BALASOORIYA, D.S., JAUHAR, T., BLAIR, A., WHEELER, C. & CHALUP, S. 2025 Layout and device parameter optimisation of a wave energy park in a broadband sea. In *The 40th International Workshop on Water Waves and Floating Bodies* (ed. X. Zhang), pp. 189–192.
WILKS, B., MONTIEL, F. & WAKES, S. 2022 Rainbow reflection and broadband energy absorption of water waves by graded arrays of vertical barriers. *J. Fluid Mech.* **941**, A26.

https://doi.org/10.1017/jfm.2026.12015

XIE, J.-J., YE, Q. & LIU, H.-W. 2025 Rainbow reflection of linear long waves excited by a finite graded array of trapezoidal bars. *Appl. Ocean Res.* **156**, 104472.

XU, J., CHEN, L., NING, D. & ZHAO, M. 2023 Resonance of water waves propagating over a uniform and a graded line array of rectified submerged cosinoidal bars. *Appl. Ocean Res.* **134**, 103531.

ZHAO, X., LI, F., ZHOU, J., GENG, J., ZOU, Q. & QIN, D. 2023 Theoretical investigation of hydrodynamic performance of multi-resonant OWC breakwater array. *Appl. Ocean Res.* **141**, 103756.

ZHOU, Z. & SONG, Z. 2025 Three-dimensional viscous study on rainbow trapping of water waves within graded cylindrical arrays. *Phys. Fluids* **37** (8), 087197.

https://doi.org/10.1017/jfm.2026.12015